Astronomy
&
Astrophysics

TOI-2257 b: A highly eccentric long-period sub-Neptune transiting a nearby M dwarf

N. Schanche[1], F. J. Pozuelos[2,3], M. N. Günther[4,5,⋆,⋆⋆], R. D. Wells[1], A. J. Burgasser[6], P. Chinchilla[2,7], L. Delrez[2,3],
E. Ducrot[2], L. J. Garcia[2], Y. Gómez Maqueo Chew[8], E. Jofré[8,9,10], B. V. Rackham[11,4,⋆⋆⋆], D. Sebastian[12],
K. G. Stassun[13], D. Stern[14], M. Timmermans[2], K. Barkaoui[2,15], A. Belinski[16], Z. Benkhaldoun[15], W. Benz[1,17],
A. Bieryla[18], F. Bouchy[19], A. Burdanov[11], D. Charbonneau[18], J. L. Christiansen[20], K. A. Collins[18],
B.-O. Demory[1], M. Dévora-Pajares[21], J. de Wit[11], D. Dragomir[22], G. Dransfield[12], E. Furlan[23], M. Ghachoui[2,15],
M. Gillon[2], C. Gnilka[24], M. A. Gómez-Muñoz[25], N. Guerrero[26,4], M. Harris[22], K. Heng[1,27], C. E. Henze[24],
K. Hesse[4], S. B. Howell[24], E. Jehin[3], J. Jenkins[24], E. L. N. Jensen[28], M. Kunimoto[4], D. W. Latham[18], K. Lester[24],
K. K. McLeod[29], I. Mireles[22], C. A. Murray[30], P. Niraula[11], P. P. Pedersen[30], D. Queloz[30], E. V. Quintana[31],
G. Ricker[4], A. Rudat[4], L. Sabin[25], B. Safonov[16], U. Schroffenegger[1], N. Scott[24], S. Seager[4,11,32], I. Strakhov[16],
A. H. M. J. Triaud[12], R. Vanderspek[4], M. Vezie[4], and J. Winn[33]

(Affiliations can be found after the references)

ABSTRACT

Context. Thanks to the relative ease of finding and characterizing small planets around M-dwarf stars, these objects have become cornerstones in the field of exoplanet studies. The current paucity of planets in long-period orbits around M dwarfs makes such objects particularly compelling as they provide clues about the formation and evolution of these systems.
Aims. In this study we present the discovery of TOI-2257 b (TIC 198485881), a long-period (35 d) sub-Neptune orbiting an M3 star at 57.8 pc. Its transit depth is about 0.4%, large enough to be detected with medium-size, ground-based telescopes. The long transit duration suggests the planet is in a highly eccentric orbit ($e \sim 0.5$), which would make it the most eccentric planet known to be transiting an M-dwarf star.
Methods. We combined TESS and ground-based data obtained with the 1.0-meter SAINT-EX, 0.60-meter TRAPPIST-North, and 1.2-meter FLWO telescopes to find a planetary size of $2.2 R_\oplus$ and an orbital period of 35.19 days. In addition, we make use of archival data, high-resolution imaging, and vetting packages to support our planetary interpretation.
Results. With its long period and high eccentricity, TOI-2257 b falls into a novel slice of parameter space. Despite the planet's low equilibrium temperature (~ 256 K), its host star's small size ($R_* = 0.311 \pm 0.015$) and relative infrared brightness ($K_{\mathrm{mag}} = 10.7$) make it a suitable candidate for atmospheric exploration via transmission spectroscopy.

Key words. planets and satellites: detection – stars: individual: TOI-2257 – stars: individual: TIC 198485881 – techniques: photometric

1. Introduction

Despite their cool temperatures, M dwarfs have become hot targets for exoplanet surveys. The large planet-to-star ratios of these systems result in relatively deep transits and large radial velocity (RV) amplitudes. In addition, they emit more strongly in the infrared. This leads to favorable conditions for atmospheric characterization by the *Hubble* Space Telescope (HST) and the *James Webb* Space Telescope (JWST). Several ground-based surveys, such as SPECULOOS (Delrez et al. 2018; Sebastian et al. 2021) and MEarth (Nutzman & Charbonneau 2008) via the transit method and CARMENES (Reiners et al. 2018) and the M-dwarf sample of HARPS (Bonfils et al. 2013) using RVs, have been created with the specific goal of finding planets around M dwarfs.

While space-based discoveries have been led by *Kepler* (Borucki et al. 2010) and K2 (Howell et al. 2014), the Transiting Exoplanet Survey Satellite (TESS; Ricker et al. 2015) is making a growing contribution to the population of planet-hosting M dwarfs, with 28 of 185 such planets discovered. Of those, only 17 are transiting planets in long-period (>15 day) orbits[1].

In this paper we present the discovery and statistical validation of a long-period sub-Neptune orbiting an M 3 star. Intriguingly, the planet's orbit is highly elliptical, suggestive of a possible perturbing outer gas giant (Huang et al. 2017; Van Eylen et al. 2019). The planet was first identified in TESS data, with further confirmation from several ground-based facilities, including three telescopes in the SPECULOOS group (Sebastian et al. 2021; Murray et al. 2020) that are designed for observations of small planets around ultra-cool M dwarfs. The planet is further validated with contributions from high-resolution imaging, spectroscopy, and archival data.

⋆ Juan Carlos Torres Fellow.
⋆⋆ ESA Research Fellow.
⋆⋆⋆ 51 Pegasi b Fellow.
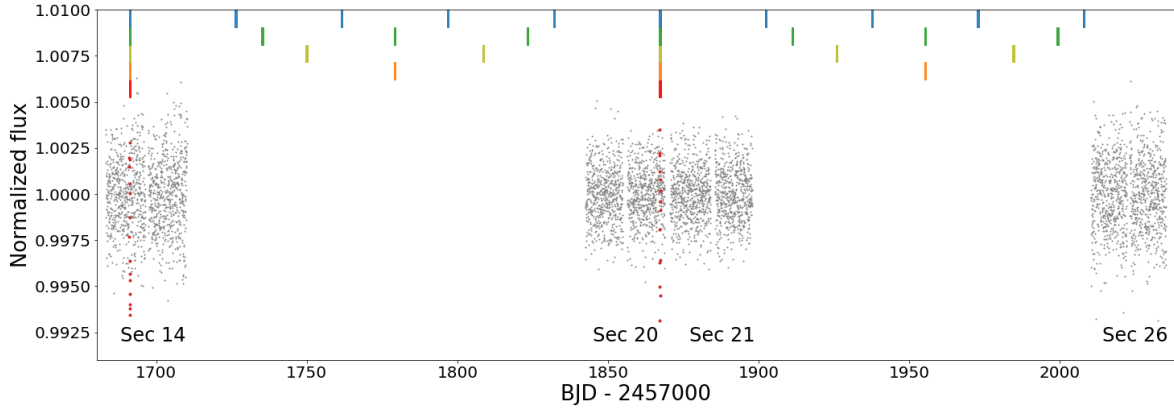
---

[1] https://exoplanetarchive.ipac.caltech.edu/

Fig. 1. Possible orbital solutions for the observed TESS transits. In-transit data points are shown in red. Based on the pattern of detections and the observation spacing, possible orbital periods include 176, 88, 59, 44, and 35 days, shown by the red, orange, mustard, green, and blue ticks, respectively.

Table 1. Ground-based photometric time-series observations of TOI-2257.

Date (UT)	Filter	Facility	Exp. time (s)	Notes
2021 April 20	$I + z$	SAINT-EX	20	Partial (egress)
2021 April 20	i'	KeplerCam	60	Partial (egress)
2021 April 20	z'	TRAPPIST-N	60	Partial (ingress)
2021 May 25	$I + z$	SAINT-EX	25	Full
2021 May 25	r'	KeplerCam	120	Partial (ingress)
2021 May 25	z'	KeplerCam	90	Partial (ingress)

The structure of the present work is as follows. In Sect. 2 we introduce the contributing facilities and data sets used in the validation of TOI-2257 b. Section 3 describes the work to characterize the host star. The analysis of the transit light curves and the characterization of the system are presented in Sect. 4. In Sect. 5 we discuss possible false-positive scenarios and argue that there is sufficient evidence for the transits to be validated as planetary in nature. The possibility of an additional planetary companion in the system is explored in Sect. 6. Finally, implications for this planet are discussed in Sect. 7.

2. Observations

In this section we present all observations of TOI-2257 taken by TESS and ground-based follow-up facilities. A summary of the photometric follow-up observations is shown in Table 1.

2.1. TESS photometry

TOI-2257 is a part of the TESS Candidate Target List (Stassun et al. 2018b) and was observed with a 2-min cadence in TESS Sectors 14 (2019 July 18–2019 August 16), 20 (2019 December 24–2020 January 21), 21 (2020 January 21–2020 February 18), and 26 (2020 June 8–2020 July 4). The image data were processed by the Science Processing Operations Center (SPOC) pipeline (Jenkins et al. 2016) to produce photometric time series. These time series were searched for transiting planet signatures with a noise-compensating matched filter (Jenkins 2002; Jenkins et al. 2010, 2020), which detected a pair of transits separated by 175 days. The transit signature passed all the diagnostic tests performed on the data (Twicken et al. 2018; Li et al. 2019), including the difference image centroid test, which located the source of the transit signature to within 1.5 ± 4.4 arcsec. No additional

transit signatures were found in the subsequent multiple planet search. The TESS Science Office reviewed the data validation reports and issued an alert for this planet candidate on 2020 August 10 (Guerrero et al. 2021).

Across the four sectors, only two transit events were detected. The separation of the two observed transits and the gaps in coverage of the object led to a possible period of 175.9 days, but other possibilities, including 88 d, 58.6 d, 44 d, and 35.2 d, could not be ruled out (see Fig. 1). From the Mikulski Archive for Space Telescopes (MAST) database, we obtained the Presearch Data Conditioning Simple Aperture Photometry (PDC-SAP; Smith et al. 2012; Stumpe et al. 2012, 2014), in which long-term trends in the data are removed. In addition, we removed all data points for which the quality flag was not 0. Figure 2 shows the apertures used for the TESS data with *Gaia* Data Release 2 (DR2) sources overlaid on the images.

2.2. Follow-up photometry

Several ground-based observations of TOI-2257 were taken in order to secure the period derived from TESS, constrain the transit parameters, and characterize the star. A non-detection on 2021 March 4 using the LCO McDonald 1-meter telescope ruled out the 58-day alias. The 35-day alias was sampled next on 2021 April 20, producing a clear transit event on three separate telescopes and securing that period solution. A further full transit was obtained during the next transit window. We describe each of these observations in the following section. The data themselves will be shown in Sect. 4.

2.2.1. LCOGT

We observed TOI-2257 in Sloan i' on UTC 2021 March 4 from the Las Cumbres Observatory Global Telescope (LCOGT; Brown et al. 2013) 1.0-meter network node at McDonald Observatory. We used the `TESS Transit Finder`, which is a customized version of the `Tapir` software package (Jensen 2013), to schedule our transit observation. The 4096 × 4096 LCOGT Sinistro cameras have an image scale of 0.″389 per pixel, resulting in a 26′ × 26′ field of view. The images were calibrated via the standard LCOGT `BANZAI` pipeline (McCully et al. 2018), and photometric data were extracted with `AstroImageJ` (Collins et al. 2017). The observation covered the 58.6-day orbital period
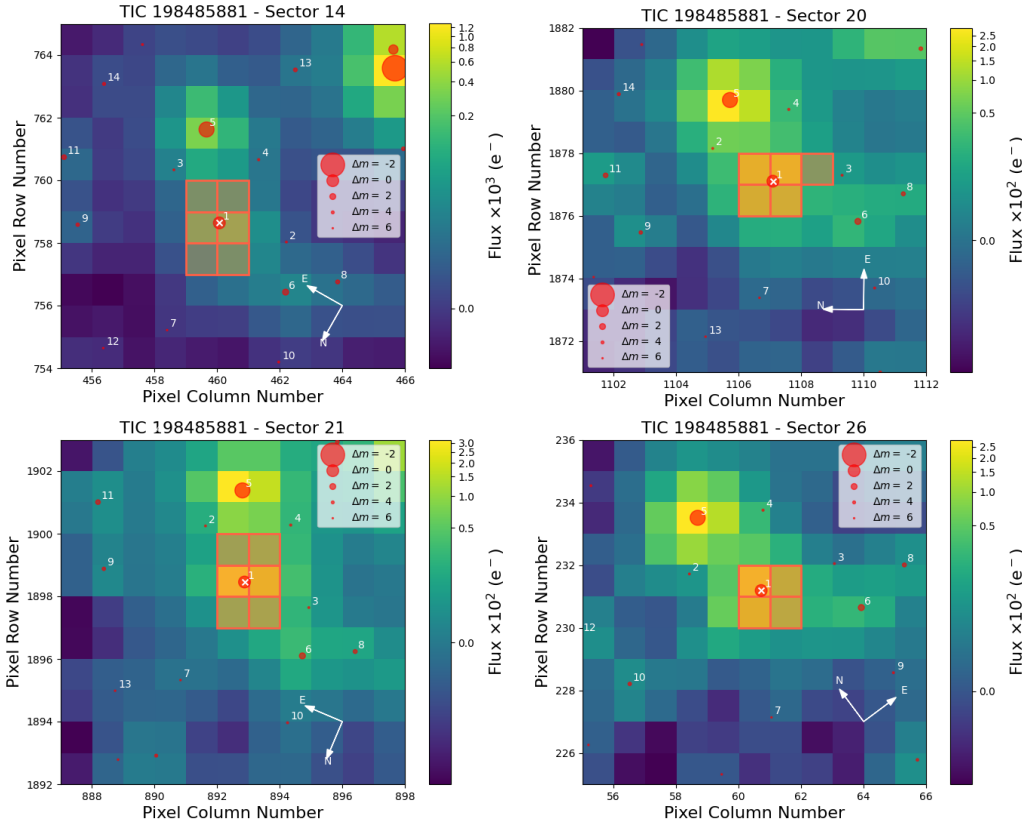
Fig. 2. TESS target pixel files of Sectors 14, 20, 21, and 26 that observed TOI-2257, generated by means of `tpfplotter` (Aller et al. 2020). The apertures used to extract the photometry by the SPOC pipeline are shown as red shaded regions. The *Gaia* DR2 catalog (Gaia Collaboration 2018) is over-plotted, with all sources of up to 6 magnitudes in contrast with TOI-2257 shown as red circles. We note that the symbol size scales with the magnitude contrast. While the star is relatively isolated, there is a small amount of contamination from outside sources, ranging from 2–5% of the total flux.

alias. The expected transit was ruled out, thus eliminating this orbital period from the list of aliases allowed by the TESS data.

2.2.2. TRAPPIST-North

We observed TOI-2257 on UTC 2021 April 20 from the TRAPPIST-North telescope, located at the Oukaïmeden observatory in Morocco (Jehin et al. 2011; Gillon et al. 2011; Barkaoui et al. 2019). TRAPPIST-North is a 0.6-meter Ritchey-Chrétien telescope equipped with an Andor charge-coupled device (CCD) camera that provides a field of view of $20' \times 20'$ with $0.60''$ pixels. This observation consisted of 369 frames of 60s exposure in the z' filter and captured the ingress of the TOI-2257 planetary candidate transit. The data were reduced using `prose` (Garcia et al. 2021), including frame alignment, calibration, and photometric extraction.

2.2.3. SAINT-EX

We used the Search And characterIsatioN of Transiting EXoplanets (SAINT-EX) Observatory (Demory et al. 2020) to obtain one partial and one full transit of TOI-2257. SAINT-EX is a 1-meter F/8 Ritchey-Chrétien telescope located at the Observatorio Astronómico Nacional in the Sierra de San Pedro Mártir, Mexico. SAINT-EX has an Andor iKon-L camera with deep-depletion e2v $2k \times 2k$ CCD optimized in the near infrared (NIR). The detector field of view is $12' \times 12'$ with $0.34''$ per pixel.

The observations were made with an I+z filter (transmittance >90% from 750 nm to beyond 1000 nm) designed for the observation of faint red targets usually observed by the SPECULOOS survey (Delrez et al. 2018; Murray et al. 2020; Sebastian et al. 2021). The first observation sequence on 2021 April 20 contained 511 observations with 20s cadence and began shortly after the expected ingress. A full transit was observed 35 days

later during the next transit window on 2021 May 25 with 402 observations using 25s cadence. Due to the low viewing angle, the telescope was reoriented shortly before egress, resulting in a slight reduction in precision in the final 84 images. The data were reduced using the custom pipeline Photometric Reduction and In-depth Nightly Curve Exploration (PRINCE; Demory et al. 2020).

2.2.4. FLWO

We observed TOI-2257 on UTC 2021 April 20 from the Fred Lawrence Whipple Observatory (FLWO) on Mt. Hopkins, Arizona, USA, using the KeplerCam CCD on the 1.2-meter telescope. KeplerCam is a 4096×4096 detector used in 2×2 binning mode that produces a $0.672''$ per pixel scale and a $23.1' \times 23.1'$ field of view. The images were reduced using standard IDL routines, and AstroImageJ was used to perform aperture photometry. We obtained 245 observations in the i' band over a period of 302 min, resulting in a clear egress detection on target.

Further observations were taken on UTC 2021 May 25 using the KeplerCam CCD in alternating z' and r' filters for a total of 44 measurements in each filter with exposure times of 90 and 120 s, respectively.

2.2.5. SPECULOOS North

In addition to observations of the transit events, we also obtained 93.5 h of observations to monitor TOI-2257 from the telescopes associated with the SPECULOOS group and located in the Northern Hemisphere; these are the SAINT-EX telescope as described in Sect. 2.2.3 and Artemis at the SPECULOOS Northern Observatory (SNO) at Teide Observatory in Tenerife (Delrez et al. 2018). The SNO data were reduced using the `prose` (Garcia et al. 2021) Python framework, and the SAINT-EX data

were reduced using the custom PRINCE pipeline. The results of this monitoring are provided in Sect. 6.2.

2.3. Spectroscopy

In order to better constrain the stellar properties, we also obtained two spectra. The results of the spectral analysis are included in Sect. 3.

2.3.1. NOT/ALFOSC

TOI-2257 was observed with the Alhambra Faint Object Spectrograph and Camera (ALFOSC) mounted on the 2.5-m Nordic Optical Telescope (NOT) at the Observatorio Roque de los Muchachos (ORM) in La Palma on 2021 June 17 in long slit spectroscopy mode. The grism used was gr5, which covers the wavelength range between 5000 and 10 700 Å, and the slit width was $1''.3$, leading to a resolution of ~320. Two exposures of 90 s were obtained. The spectroscopic standard star SP1446+259 was also observed to correct for instrumental response. Some bias, flat field, and arc images were also acquired for the reduction and calibration of the spectra.

The reduction was performed using IRAF standard routines, which included bias subtraction, flat field correction, wavelength calibration, and extraction of the spectra. The instrumental response was corrected using the spectrum of the spectroscopic standard star. The spectra were not corrected for atmospheric telluric absorptions.

2.3.2. DBSP

We observed TOI-2257 on UTC 2021 June 16 from the Hale 200″ telescope at Palomar Observatory using the dual-beam optical Double Spectrograph (DBSP). The observations suffered from variable cloud cover, and seeing at the start of the night was ~ $1''.5 - 2''.0$. We obtained two 450 s observations using the $1''.5$ slit, the 5600Å dichroic, the 600 ℓ mm^{-1} blue grism ($\lambda_{blaze} = 4000$ Å), and the 400 ℓ mm^{-1} red grating ($\lambda_{blaze} = 8500$ Å). This instrument configuration covers the full optical window at moderate resolving power, $R \approx 1000$, with a modest gap at the dichroic. Relative flux calibration was obtained using observations of the subdwarf O star HZ44 from Massey & Gronwall (1990) obtained on the same night. The spectra were reduced using standard IRAF routines.

2.4. High-resolution imaging

Two high angular resolution images were taken as part of the TESS Follow-up Observing Program (TFOP) in order to rule out false positives caused by possible unresolved stellar companions or detect any close companions that could dilute the transit signal and lead to an underestimation of the planet radius. These observations are presented below.

2.4.1. SPP speckle interferometry

TOI-2257 was observed using speckle interferometry on 2020 November 29 with the SPeckle Polarimeter (SPP; Safonov et al. 2017) on the 2.5-m telescope at the Sternberg Astronomical Institute of Lomonosov Moscow State University (SAI MSU). The SPP uses Electron Multiplying CCD Andor iXon 897 as a detector with a pixel scale of 20.6 mas px^{-1}. The observation was made in the I band, and the atmospheric dispersion was compensated for. The angular resolution was 89 mas. The detection
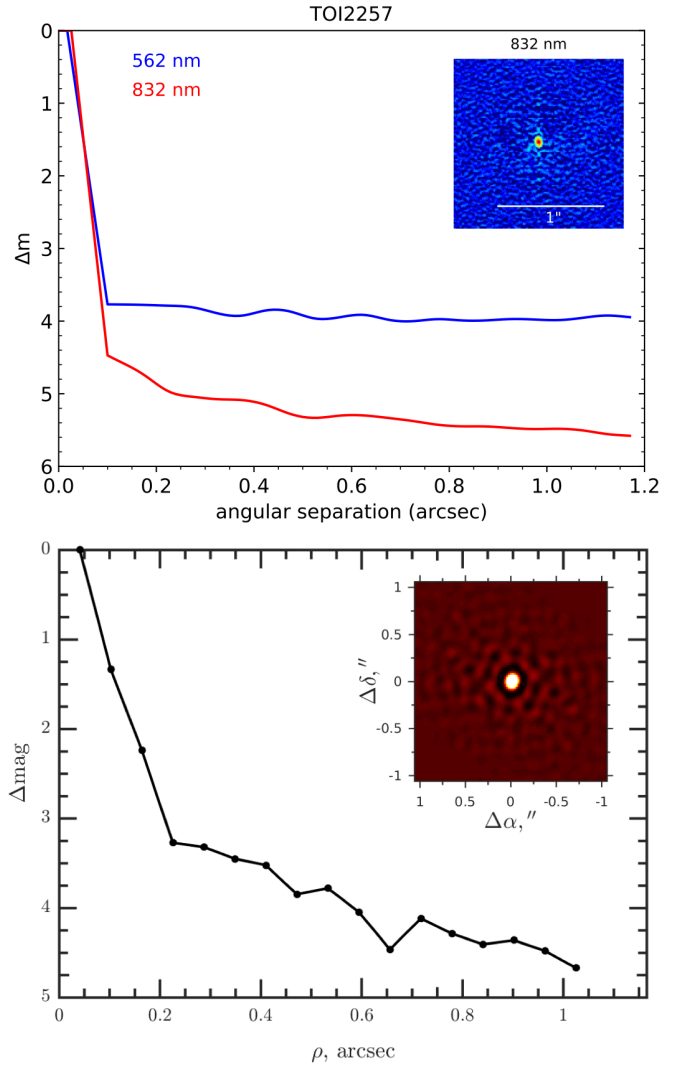
Fig. 3. Contrast curves for TOI-2257 b from high angular resolution imaging. The *top plot* shows the results of the Alopeke speckle instrument on Gemini North. The *bottom plot* shows the speckle interferometry taken by SPP at the Sternberg Astronomical Institute. Both plots have the final reconstructed image inlaid in the upper right. Neither instrument detects a nearby companion with a magnitude within 4.5 mags of the target star.

limit for faint stellar companions is provided in Fig. 3. We did not detect any companion brighter than this limit (e.g., 4.5 mag at 1″).

2.4.2. Alopeke speckle imaging

TOI-2257 was observed on UT 2021 February 2 using the 'Alopeke speckle instrument on Gemini North[2] (Scott et al. 2021). 'Alopeke provides simultaneous speckle imaging in two bands (562 and 832 nm) with output data products that include a reconstructed image with robust contrast limits on companion detections (e.g., Howell et al. 2016). Eight sets of 1000 X 0.06 sec exposures were collected and subjected to Fourier analysis in our standard reduction pipeline (see Howell et al. 2011). Figure 3 shows our final contrast curves and the 832 nm reconstructed speckle image. We find that TOI-2257 is a single star with no companion brighter than about 4.5–5 magnitudes below

---

[2] https://www.gemini.edu/sciops/instruments/alopeke-zorro/

that of the target star from the diffraction limit (20 mas) out to 1.2″. At the distance of TOI-2257 (d = 57.8 pc), these angular limits correspond to spatial limits of 1–69 au.

3. Stellar properties

3.1. Spectroscopic analysis

Based on the Palomar/DBSP and NOT/ALFOSC spectra, we constrained the fundamental properties of TOI-2257 from the analysis of molecular band indices.

We estimated the effective temperature, T_{eff}, employing the relationship between this parameter and the CaH_2 index obtained for M dwarfs derived by Woolf & Wallerstein (2006). We obtained T_{eff} = 3277 ± 250 K (CaH_2 = 0.36) and T_{eff} = 3395 ± 310 K (CaH_2 = 0.43) for the NOT/ALFOSC and Palomar/DBSP data, respectively. These values are in good agreement with those obtained from the optical and infrared photometric calibration of Casagrande et al. (2008), which yields T_{eff} = 3279 ± 51 K for (V−Ks) and T_{eff} = 3266 ± 30 K for (V−J).

Based on the band strength indices CaH_2, CaH_3, and TiO_5, we computed the coarse metallicity parameter $\zeta_{TiO/CaH}$ (ζ for short), as described by Lépine et al. (2007). Then, we used the relation between this parameter and the [Fe/H] derived by Mann et al. (2013) to obtain [Fe/H] = −0.29 ± 0.31 (ζ = 0.76 ± 0.3) and [Fe/H] = −0.23 ± 0.5 dex (ζ = 0.76 ± 0.3) for the NOT/ALFOSC and Palomar/DBSP data, respectively. These values are in good agreement with the results obtained from photometric calibrations. We derived [Fe/H]= −0.35 ± 0.18 dex for the (V−Ks) calibration of Schlaufman & Laughlin (2010), [Fe/H] = −0.23 ± 0.22 dex for the (V−Ks) calibration of Mann et al. (2013), and [Fe/H] = −0.23 ± 0.20 dex for the (Bp−Ks) calibration of Rains et al. (2021).

We derived several gravity-sensitive spectral indices to establish the main-sequence dwarf nature of TOI-2257. We computed the gravity-sensitive indices Na_{8189} and TiO_{7140}, which, as shown by several authors, clearly separate low, intermediate, and high gravity for spectral types later than M 2 (e.g., Slesnick et al. 2006). The measured spectral indices for the NOT/ALFOSC data are TiO_{7140} = 1.40 and Na_{8189} = 0.94, whilst for the Palomar/DBSP we obtained TiO_{7140}= 1.38 and Na_{8189} = 0.91. These values place TOI-2257 in the high surface gravity region (dwarf stars) around the M3 spectral types in Fig. 11 of Slesnick et al. (2006). As expected, a visual inspection of the spectra of TOI-2257 reveals a clear absorption by the NaI doublet at 8183 and 8195 Å, which is not seen in giant stars. Furthermore, as in Alonso-Floriano et al. (2015), we computed the index Ratio C, which is also highly sensitive to surface gravity. We derived Ratio C = 1.15 and Ratio C = 1.23 for the NOT/ALFOSC and Palomar/DBSP data, respectively. These values place TOI-2257 in the high surface gravity field-dwarf region in Fig. 6 of Alonso-Floriano et al. (2015), which is well above the limit of giant stars at Ratio C = 1.07.

Finally, we assessed the spectral type of TOI-2257 using the PYHAMMER tool[3] (Kesseli et al. 2017), which estimates MK spectral types by comparing our data with reference spectra of M-type stars (Covey et al. 2007). The best fit is obtained for an M3V star with [Fe/H] ∼ 0 dex. Moreover, as in Slesnick et al. (2006), we computed the temperature-sensitive index TiO_{8465}, in addition to the TiO_{7140} index presented above, obtaining TiO_{8465} = 1.16 and TiO_{8465} = 1.07 for the NOT/ALFOSC and Palomar/DBSP data, respectively. These values locate TOI-2257
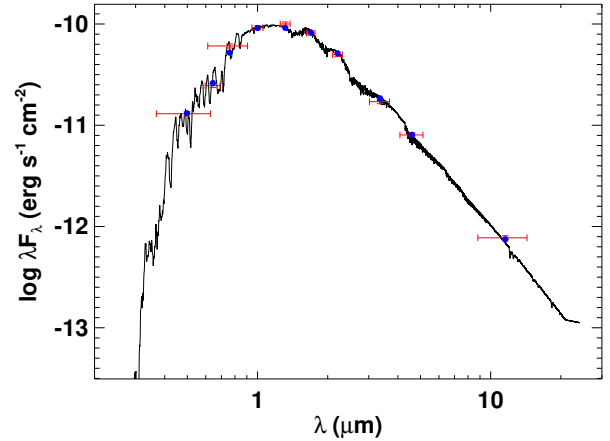
---

[3] https://github.com/BU-hammerTeam/PyHammer

Fig. 4. SED of TOI-2257. The red symbols represent the observed photometric measurements; the horizontal bars represent the effective width of the passband. The blue symbols are the model fluxes from the best-fit NextGen atmosphere model (black).

around the M3 spectral type region in Fig. 9 of Slesnick et al. (2006).

3.2. SED fitting and evolutionary modeling

As an independent determination of the basic stellar parameters, we performed an analysis of the broadband spectral energy distribution (SED) of the star together with the *Gaia* Early Data Release 3 (EDR3; Stassun & Torres 2021) parallax (with no systematic correction) in order to determine an empirical measurement of the stellar radius, following the procedures described in Stassun & Torres (2016); Stassun et al. (2017, 2018a). We pulled the JHK_S magnitudes from 2MASS, the W1–W3 magnitudes from WISE, the $GG_{BP}G_{RP}$ magnitudes from *Gaia*, and the *gry* magnitudes from Pan-STARRS. Together, the available photometry spans the full stellar SED over the wavelength range 0.4–10 μm (see Fig. 4).

We performed a fit using NextGen stellar atmosphere models (Hauschildt et al. 1999), with the effective temperature (T_{eff}), surface gravity ($\log g$), and metallicity ([Fe/H]) adopted from the spectroscopic analysis. The remaining free parameter is the extinction, A_V. The resulting fit (Fig. 4) has a reduced χ^2 of 1.6, with best fit A_V = 0.03 ± 0.03. Integrating the (un-reddened) model SED gives the bolometric flux at Earth, F_{bol} = 1.168 ± 0.041 × 10^{-10} erg s^{-1} cm^{-2}. Taking the F_{bol} and T_{eff} together with the *Gaia* parallax gives the stellar radius R_* = 0.311 ± 0.015 $R_\odot$. Finally, the absolute M_K magnitude together with the empirical relations of Mann et al. (2019) implies a stellar mass of M_* = 0.33 ± 0.02 $M_\odot$. Together with the empirical radius above, this in turn yields a mean stellar density of ρ_* = 15.7 ± 2.5 g cm^{-3} and a surface gravity of $\log g$ = 4.971 ± 0.050.

We also estimated the stellar properties using a complementary, isochrone-dependent approach. For this analysis, we used the `isochrones` software package (Morton 2015), which can be used to fit data inputs to the MESA Isochrones and Stellar Tracks database (Dotter 2016; Choi et al. 2016) via the nested sampling algorithm MULTINEST (Feroz et al. 2009) as implemented in the `PyMultiNest` package (Buchner et al. 2014). We used as inputs the stellar metallicity from Table 2, the BV magnitudes tabulated in the revised TESS Input Catalog (TIC; Stassun et al. 2019), the JHK_s magnitudes from 2MASS (Skrutskie et al. 2006; Cutri et al. 2003), and the W1–W3 magnitudes from WISE

Table 2. Properties of the host star.

Parameter	Value	Source
	Designations	
TIC	198 485 881.01	
2MASS	J12585767+7739416	
Gaia DR2	1 716 345 832 872 291 968	
UCAC 4	839-012174	
	Photometric magnitudes	
TESS	12.9672 ± 0.0074	[1]
B	16.648 ± 0.098	[1]/[2]
V	15.211 ± 0.034	[1]/[2]
g'	15.990 ± 0.242	[2]
r'	14.599 ± 0.057	[2]
i'	13.345 ± 0.177	[2]
Gaia	14.1615 ± 0.000437	[3]
J	11.47 ± 0.018	[1]/[4]
H	10.89 ± 0.015	[1]/[4]
K	10.673 ± 0.016	[1]/[4]
WISE 3.4 μm	10.514 ± 0.023	[5]
WISE 4.6 μm	10.355 ± 0.02	[5]
WISE 12 μm	9.972 ± 0.039	[5]
WISE 22 μm	8.601 ± 0.244	[5]
	Stellar properties	
RA (J2000)	12:58:57.51	[1]
Dec (J2000)	+77:39:42.18	[1]
pm (RA) mas yr^{-1}	-36.035 ± 0.021	[6]
pm (Dec) mas yr^{-1}	31.408 ± 0.018	[6]
Parallax mas	17.283 ± 0.015	[6]
Distance pc	$57.7911^{+0.1053}_{-0.1049}$	[7]
Spectral type	M3	[8]
$T_{\rm eff}$/ K	3430 ± 130	[8]
[Fe/H]	-0.27 ± 0.37	[8]
$M_*/M_\odot$	0.33 ± 0.02	[8]
$R_*/R_\odot$	0.311 ± 0.015	[8]
$\log g$ / dex	4.971 ± 0.050	[8]
$\rho_*/{\rm g\,cm^{-3}}$	15.8 ± 2.5	[8]
$F_{\rm bol}/{\rm erg\,s^{-1}cm^{-2}}$	$(1.171 \pm 0.055) \times 10^{-10}$	SED

References. 1: TIC (Stassun et al. 2018b), 2: APASS-dr9 (Henden et al. 2015), 3: *Gaia* DR2 (Gaia Collaboration 2018), 4: Catalog of Cool Dwarf Targets (Muirhead et al. 2018), 5: WISE (Cutri et al. 2021), 6: *Gaia* DR3 (Gaia Collaboration 2021), 7: Bailer-Jones et al. (2018), 8: see Sect. 3.3.

(Wright et al. 2010) as well as the *Gaia* EDR3 parallax (Gaia Collaboration 2016, 2021). This analysis gives a stellar effective temperature of $T_{\rm eff} = 3441 \pm 19$ K, a surface gravity of $\log g = 4.926 \pm 0.054$, a mass of $M_* = 0.315 \pm 0.028\,M_\odot$, a radius of $R_* = 0.3190 \pm 0.0024$, and a density of $\rho_* = 13.7 \pm 1.3\,{\rm g\,cm^{-3}}$, which is in line with the results of the SED fitting. The results also favor a stellar age of ≥ 8.0 Gyr at 3σ and minimal line-of-sight extinction ($A_{\rm V} < 0.2$ at 3σ). While we note the consistency of the isochrone-derived parameter values with the others presented here, we do not include them in the calculation of the final, adopted stellar parameters as the uncertainties are likely underestimated.

3.3. Adopted stellar parameters

We compiled our final set of adopted stellar parameters from the analyses of the NOT/ALFOSC and Palomar/DBSP spectra and

the SED. In particular, the analyses detailed previously yielded three estimates of $T_{\rm eff}$ (from NOT/ALFOSC, Palomar/DBSP, and the SED analyses) and two estimates of [Fe/H] (from the NOT/ALFOSC and Palomar/DBSP analyses). For each parameter, we calculated the weighted mean of the estimates using a Monte Carlo approach. We drew a total of 10^6 samples from normal distributions with the means and standard deviations of the estimates, using inverse-variance weighting to determine the number of subsamples to draw from each distribution. We then calculated the mean and standard deviation of the resulting sample. We adopted these values as our final estimates of $T_{\rm eff}$ and [Fe/H], which are presented in Table 2.

4. Transit analysis

In this section we outline the fit of the data to a transit model as well as an analysis of possible transit timing variations (TTVs).

4.1. Transit model fit

All the light curves described in Sect. 2 were used simultaneously to fit the transit using a Markov chain Monte Carlo (MCMC) approach. We employed the PyTransit (Parviainen 2015) implementation of the Mandel & Agol (2002) quadratic limb darkening transit model, with sampling done using emcee (Foreman-Mackey et al. 2013), a Python implementation of the affine invariant MCMC ensemble sampler (Goodman & Weare 2010). The parameters used for the transit model are the planet-to-star radius ratio R_p/R_*, the impact parameter b, the zero epoch T_0, the period P, and the stellar mass and radius M_* and R_*. The eccentricity and argument of periastron were fit using the parameterization of $\sqrt{e}\cos\omega$ and $\sqrt{e}\sin\omega$. In addition, two quadratic limb darkening parameters were fit for each wavelength. The ground-based data were simultaneously detrended using an out-of-transit baseline as well as quadratic terms for the airmass and full width at half maximum (FWHM) trends. Priors used for the analysis are shown in Table 3.

The final transit model is shown in Fig. 5 over the detrended light curves. The posterior distributions for the transit parameters can be found in Appendix A.1, and the final fit and derived parameters for the planetary system can be found in Table 3. While we currently have no mass estimations from RV measurements, we used the relationship in Chen & Kipping (2017) to estimate a range of likely values. The RV semi-amplitude could thus be estimated, leading to an expected signal around 3.5 m s^{-1}.

We also carried out an independent analysis using the juliet package (Espinoza et al. 2019), which is built over batman (Kreidberg 2015) for the modeling of transits and the dynesty (Speagle 2020) dynamic nested sampling algorithm for estimating Bayesian posteriors and evidence. The fit transit parameters were: R_p/R_*, b, T_0, P, the stellar density ρ_*, $\sqrt{e}\cos\omega$, and $\sqrt{e}\sin\omega$. For each passband, we also fit two quadratic limb-darkening coefficients, which were parameterized using the (q_1, q_2) triangular sampling scheme of Kipping (2013). All these parameters were sampled from wide uniform priors, except the stellar density, for which we used a normal prior based on the value and uncertainty reported in Table 2.

We first performed individual analyses of each of our light curves, in order to select for each of them the best correlated noise model based on Bayesian evidence. We explored a large range of models, consisting of first- to fourth-order polynomials with respect to, for example, time, airmass, point spread function (PSF) FWHM, background, stellar position on the detector,

Table 3. Fit and derived parameters for the TOI-2257 b system.

Parameter	Unit	Value	Prior
Fitted parameters			
Orbital period P	days	35.189346(90)	$\mathcal{N}(35.189295, 1e-4)$
Mid-transit time T_0	BJD-2 450 000	$9007.97949^{+0.00108}_{-0.00105}$	$\mathcal{N}(9007.978906, 0.1)$
$(R_{\rm p}/R_*)$		$0.06423^{+0.00142}_{-0.00133}$	$\mathcal{U}(0.001, 0.4)$
Impact parameter b		$0.374^{+0.098}_{-0.137}$	$\mathcal{U}(0, 1)$
$\sqrt{e}\sin\omega$		$-0.615^{+0.083}_{-0.073}$	$\mathcal{U}(-1, 1)$
$\sqrt{e}\cos\omega$		$-0.126^{+0.484}_{-0.387}$	$\mathcal{U}(-1, 1)$
Stellar mass M_*	$M_\odot$	$0.328^{+0.021}_{-0.019}$	$\mathcal{N}(0.33, 0.02)$
Stellar radius R_*	$R_\odot$	0.313 ± 0.015	$\mathcal{N}(0.311, 0.015)$
Physical and orbital parameters			
Planet radius $R_{\rm p}$	$R_\oplus$	$2.194^{+0.113}_{-0.111}$	
Orbital eccentricity e		$0.496^{+0.216}_{-0.133}$	
Argument of periastron ω	°	$-101.674^{+42.453}_{-26.881}$	
Semimajor axis a	au	0.145 ± 0.003	
Inclination i	°	$89.786^{+0.078}_{-0.062}$	
Equilibrium temperature $T_{\rm eq}$ [*]	K	256^{+61}_{-17}	
Depth δ		$0.00413^{+0.00018}_{-0.00017}$	
Transit duration	h	$3.846^{+0.057}_{-0.051}$	
Predicted parameters			
Planet mass $M_{\rm p}$	$M_\oplus$	$5.712^{+4.288}_{-2.311}$	
RV Semi-amplitude K	m s^{-1}	$3.521^{+2.901}_{-1.507}$	
TSM		$32.708^{+24.08}_{-14.362}$	
Limb darkening			
q1 (TESS)		0.328 ± 0.008	$\mathcal{N}(0.3281, 0.0079)$
q2 (TESS)		0.203 ± 0.022	$\mathcal{N}(0.2020, 0.0229)$
q1 ($I+z$)		0.289 ± 0.008	$\mathcal{N}(0.2903, 0.0076)$
q2 ($I+z$)		$0.193^{+0.027}_{-0.026}$	$\mathcal{N}(0.1992, 0.0260)$
q1 (i')		$0.385^{+0.01}_{-0.009}$	$\mathcal{N}(0.3849, 0.0098)$
q2 (i')		0.213 ± 0.03	$\mathcal{N}(0.2070, 0.0301)$
q1 (z')		$0.300^{+0.008}_{-0.009}$	$\mathcal{N}(0.2994, 0.0088)$
q2 (z')		$0.206^{+0.034}_{-0.031}$	$\mathcal{N}(0.2050, 0.0327)$
q1 (r')		$0.568^{+0.012}_{-0.011}$	$\mathcal{N}(0.5686, 0.0116)$
q2 (r')		0.164 ± 0.034	$\mathcal{N}(0.1663, 0.0326)$

Notes. [*]Time-averaged equilibrium temperature taking into account the eccentric orbit using the formulation of Méndez & Rivera-Valentín (2017), assuming zero albedo and full day-night heat redistribution.

or any combination of these parameters. First- or second-order polynomials of airmass and/or FWHM were typically favored. For each light curve, we also fit a jitter term, which was added quadratically to the error bars of the data points, to account for any underestimation of the uncertainties or any excess noise not captured by our modeling.

We then conducted two global analyses: one assuming a circular orbit (e set to zero) and one allowing the orbit of the planet to be eccentric. Following Espinoza et al. (2019), we found the eccentric model ($e = 0.41^{+0.21}_{-0.12}$) to be strongly favored over the circular one, with a difference in Bayesian log evidence ($\Delta \ln Z$) of 5.2 (i.e., posterior odds of $\approx$180 : 1 assuming equiprobable

models), lending substantial support to our eccentric interpretation (Kass & Raftery 1995). All transit parameters returned by the eccentric fit are consistent within the uncertainties with the ones reported in Table 3.

4.2. Transiting timing variations

Transit timing variations are of interest in this context because they can point to the existence of other planets in the system and can potentially be used to constrain the mass of the transiting planet. We investigated the evidence for TTVs of TOI-2257 b in a separate analysis of the transit light curves, generating the
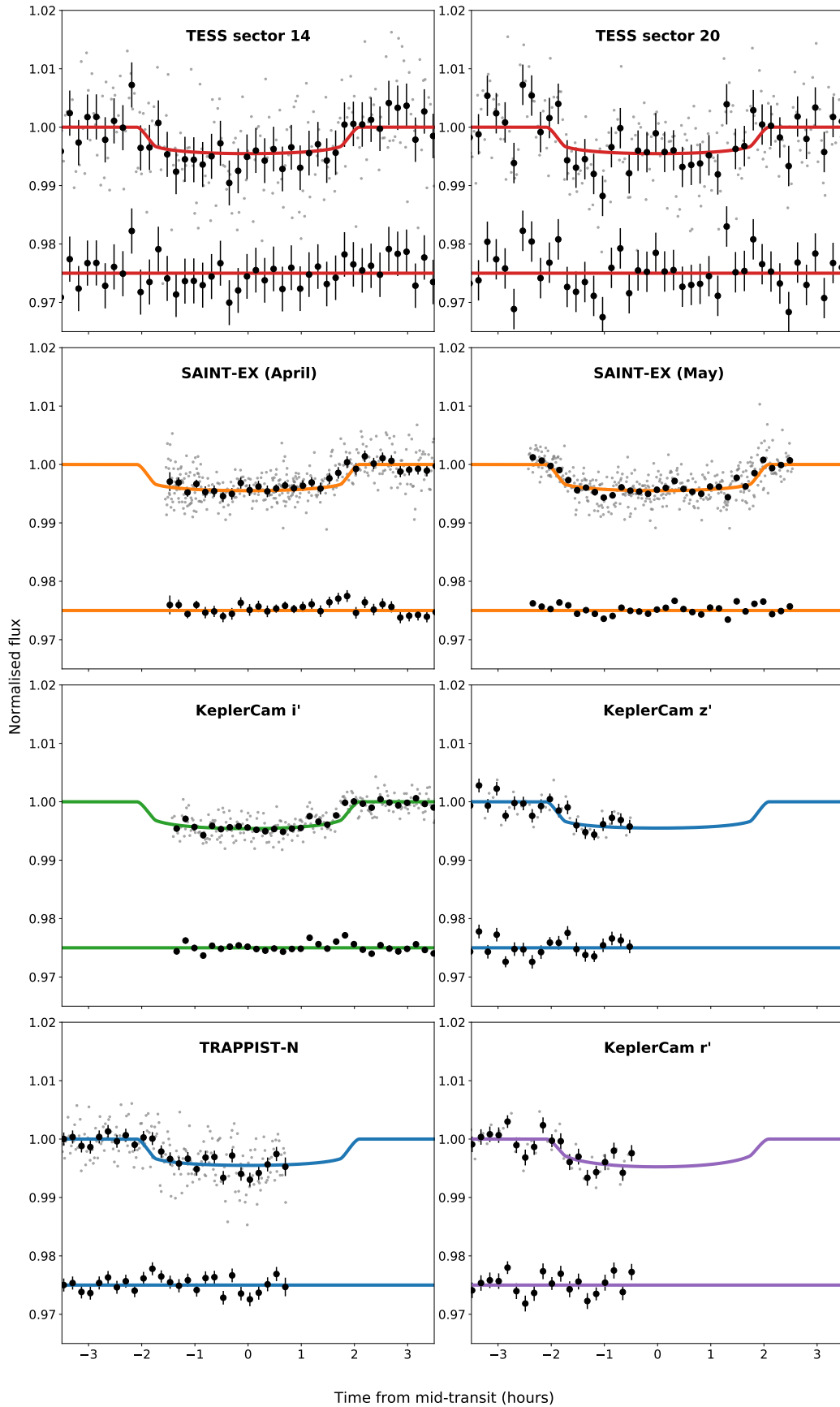
Fig. 5. Photometric observations of TOI-2257 with the best-fit transit parameters over-plotted. Thick black points show 10-min bins, with all data points shown in gray. Residuals from the model fit are shown with an arbitrary offset below the transit. It should be noted that, for the sake of clarity, only 10-min-binned residuals are shown. The color of the line reflects the filter used for the observations (red for TESS, orange for I+z, green for *i'*, blue for *z'*, and purple for *r'*).
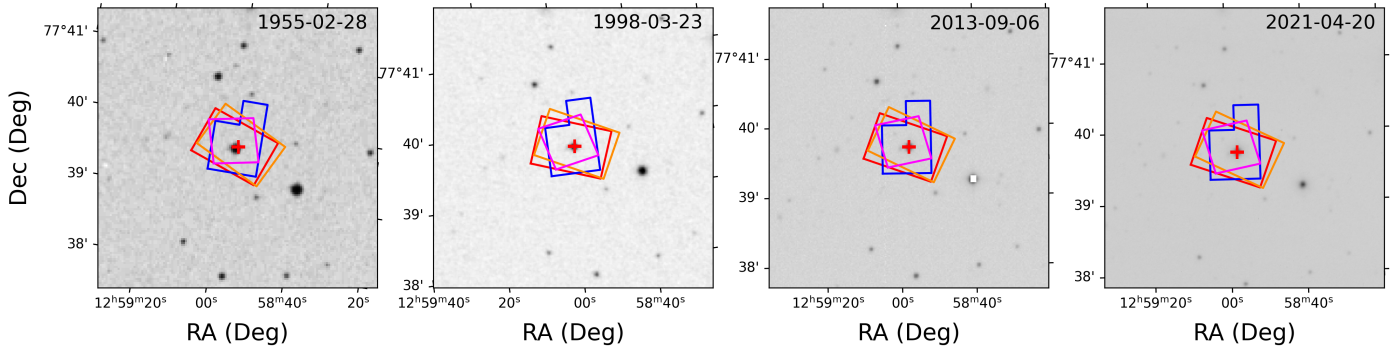
Fig. 6. Archival images around TOI-2257 with TESS's apertures used in Sectors 14 (red), 20 (blue), 21 (yellow) and 26 (magenta) superimposed to assess for current, unresolved blending. *From left to right*: (1) 1955 February 28 DSS1-red filter, (2) 1998 March 23 DSS2-red filter, (3) 2013 September 06 PTF-red filter, and (4) 2021 April 20 TN-red filter. Its current location (red cross) is marked in all images.

TTV light curve model with the `exoplanet` software package (Foreman-Mackey et al. 2021a) and performing the posterior inference with the `PyMC3` software package (Salvatier et al. 2016). Our approach was similar to those of other recent TTV analyses of TESS-discovered exoplanets (Badenas-Agusti et al. 2020; Daylan et al. 2021).

As data inputs, we used TESS Sector 14 and 20 two-minute-cadence light curves, the 2021 April 20 partial-transit light curves from SAINT-EX, KeplerCam, and TRAPPIST-N, and the 2021 May 25 full-transit light curve from SAINT-EX, the most constraining data on this particular transit. We placed normal priors on the stellar mass and radius using the values presented in Table 2 and on the planet-to-star radius ratio and period using the values presented in Table 3. We placed uninformative priors on the impact parameter and the quadratic limb-darkening coefficients using the physical distributions built into `exoplanet`, the latter of which relies on the triangular sampling method of Kipping (2013). We placed a normal prior on the period of the planet using the results of the linear-ephemeris analysis and uniform priors on the times of the four observed transits, centered on the expected transit times from the linear ephemeris and with a width of 1 h. Finally, we placed a normal prior on the out-of-transit flux for all data sets, centered on the median flux value and using a standard deviation that is robustly estimated using the median absolute deviation of the fluxes.

This model has some notable simplifications. We assumed that the noise is normally distributed and did not attempt to model any residual systematics in the normalized light curves. Since all the observations are generally in the red optical, we also used a single set of limb-darkening coefficients and a single transit depth to model the light curve despite the somewhat different bandpasses of the observations. Finally, we used a single out-of-transit flux value for the combined data set, assuming that any errors in the normalization of the individual data sets are negligible. These simplifications notably reduce the complexity of the model and improve the computational efficiency of the sampling, and we assume that they do not significantly impact the inference of the transit times.

We find that the four transits are consistent with a linear ephemeris at the 1σ level with inferred TTVs of 1.5 ± 4.7, -2.0 ± 6.4, 0.3 ± 1.1, and 0.3 ± 1.2 min. The smaller uncertainties of the last two transits illustrate the improved timing estimates afforded by our ground-based follow-up observations. We conclude that the existing observations do not show any evidence of TTVs. TESS observations of TOI-2257 in the near future (in Sectors 40, 41, 47, 48, and 53) can be monitored to check if any potential variations emerge.

5. Planet validation

5.1. TESS data validation report

The natural first step for false-positive vetting was to closely analyze the TESS data validation report (Twicken et al. 2018; Li et al. 2019) based on the 176-day solution. All tests, including those for odd-even transit depths, centroid shifts, and "ghosts", produced favorable results. The encouraging results led to further follow-up in the system.

5.2. Follow-up photometry

The TESS data validation report indicates that there is one contaminating source within the TESS apertures used in both Sectors 14 and 20 at a distance of 16.47″. We identify this as the faint source with *Gaia* ID 1716345832871506560 (*G*-mag 20.7). The pixel scale from the ground-based follow-up photometry extracted light curves using an aperture of only a few arcseconds, and therefore we were able to resolve the target in isolation. No transit event was seen on this faint star or any other nearby star, while a dimming event was clearly observed on the target.

5.3. Archival imaging

We used archival images to investigate the contamination of background stars (e.g., Quinn et al. 2019). We aimed to rule out the presence of eclipsing binaries (EBs) at the present-day target location, which might introduce transit-like signals in the data. Unfortunately, TOI-2257 has a moderately low proper motion of ~ 0.047 arcsec yr^{-1}. The oldest archival image that we found was taken in 1955, 64 and 66 yr before the first and the last TESS observations in Sectors 14 and 26, respectively. This oldest archival image has a pixel scale and PSF of 1.69 arcsec pixel^{-1} and 8.05 arcsec, respectively. Since that time, the star has only moved ~ 3.1 arcsec (see Fig. 6). While it seems that there is not any background star that might be producing the transit-like signals detected in our data, we cannot confidently rule out that possibility. We would need to wait for ~ 150 yr to reach a separation of 10 arcsec since 1955, a distance larger than the 1955 PSF that would allow us to confidently rule out the contamination caused by a background EB.

5.4. False-positive likelihood

To assess the possibility that the observed transit was not due to a planet orbiting the target star, but rather from an astrophysical false-positive scenario, we used the software package

triceratops (Giacalone et al. 2021). This package was developed as a tool to assist in the vetting and validation of TESS candidates (see, e.g., Cloutier et al. 2020; Demory et al. 2020; Hedges et al. 2021; Wells et al. 2021). Using a Bayesian framework, triceratops calculates the probability that the signal is caused by a variety of true-positive or false-positive scenarios. The calculations incorporate prior knowledge about the target star, exoplanet occurrence rates, and stellar multiplicity. One metric that is returned is the false-positive probability (FPP), which is the sum of probabilities for all false-positive scenarios. Using the TESS 2-min data from Sectors 14 and 20 gives an FPP of 0.078 ± 0.009. However, triceratops is also able to incorporate additional information from contrast curves to further constrain the false-positive scenarios. By incorporating this information, the FPP is reduced to 0.0255 ± 0.0012. However, the higher precision of the SAINT-EX light curve is more constraining than the TESS data. We therefore modified the input to triceratops to use the detrended SAINT-EX transit observation from May 25 along with the contrast curve, reducing the FPP to a negligible value ($\sim 8.7 \times 10^{-9}$). We are therefore able to statistically validate this object as a planet.

5.5. Unresolved stellar companions

Based on the high-resolution imaging (see Sect. 2.4), we ruled out the potential for a companion within 4.5–5.5 mag of the target star outside 6 au at 832 nm, which corresponds to a magnitude of 18.6 in the r' band. Theory and observations established that the mass cutoff for what constitutes a star is different for objects of different metallicity. For objects with a solar-like metallicity, anything with less than $0.075\,M_\odot$ will be a brown dwarf (Boss 2001), while for objects with lower metallicity, the mass limit will be about $0.083\,M_\odot$ (Richer et al. 2006). Using the models by Baraffe et al. (2015) and assuming a stellar age of 5 Gyr, we found an upper limit for the companion's mass of $0.075\,M_\odot$. Hence, this result allows us to confidently rule out the presence of an unresolved stellar companion. Nevertheless, substellar objects with masses ranging from $0.01–0.075\,M_\odot$ would still be possible.

6. Planet searches and detection limits

6.1. TESS photometry

To search for additional planets, we used our custom pipeline SHERLOCK[4] (Pozuelos et al. 2020; Demory et al. 2020). SHERLOCK is a user-friendly open-source package that has five different modules that allow the user to: (1) search for planetary candidates; (2) perform vetting of the most promising signals; (3) compute a statistical validation; (4) model the signals to refine the ephemerides; and (5) compute the observational windows from ground-based observatories. SHERLOCK has direct access to short- and long-cadence data observed by *Kepler*/K2 and TESS. Hence, SHERLOCK is a fully operational, powerful tool that allows users to perform the planet search fast and robustly.

SHERLOCK applies a multi-detrend approach to the nominal light curve, employing the wōtan package (Hippke et al. 2019), that is, the nominal light curve is detrended several times using a bi-weight filter by varying the window size. This strategy allows

the user to maximize the signal detection efficiency (SDE) and the signal-to-noise ratio (S/N) of the transit search, which is performed over the nominal light curve, jointly with the new detrended light curves, through the transit least squares (TLS) package (Hippke & Heller 2019). TLS is optimized to detect shallow periodic transits using an analytical transit model based on the stellar parameters. The transit search is performed in a loop; once a signal is found, it is recorded and masked, and then the search keeps running until no more signals with $S/N \geqslant 5$ are found in the data set. To start the search for extra planets, we masked the transits corresponding to the candidate TOI-2257 b, with an orbital period of 35.19 d, $T_0 = 1691.28$ d, and $T_{14} = 228$ min. Then, we performed three transit searches, firstly by considering all the sectors available simultaneously, that is, combining Sectors 14, 20, 21, and 22. We focused our search for orbital periods ranging from 0.5 to 30 d, where at least two transits were required to identify a potential signal. Secondly, we focused on the longer orbital periods, ranging from 40 to 80 d. In this case, we allowed single transits to be recovered. Finally, we explored all the sectors independently, focusing on orbital periods ranging from 0.5 to 15 d. This strategy allowed us to avoid having sectors with different photometric precision affect the global search.

After the scrutiny of the data, we found no clear evidence of additional planetary transits. All the signals found by SHERLOCK were attributable to systematics, noise, or variability. Following Wells et al. (2021), the lack of detections of extra signals suggests that: (1) no other planets exist in the system; (2) if they do exist, they do not transit; or (3) they exist and transit, but the photometric precision of the data set is not good enough to detect them, or they have periods longer than the ones explored in this study. If scenario (2) or (3) is true, extra planets might be detected by RV follow-up, as discussed in Sect. 7.

To evaluate scenario (3), we studied the detection limits of the current data set by performing injection-and-recovery experiments over the PDC-SAP light curves, combining the four sectors available. To this end, we used the MATRIX ToolKit[5].

MATRIX ToolKit allows the user to define the ranges in the $R_{\mathrm{planet}}-P_{\mathrm{planet}}$ parameter space to be examined. Each combination of $R_{\mathrm{planet}}-P_{\mathrm{planet}}$ is explored using a number of different phases, that is, different values of T_0. For simplicity, it is assumed that the impact parameters and eccentricities of the injected planets are zero. To perform the injection-and-recovery experiments, MATRIX ToolKit injected the synthetic planets, detrended the light curves using a bi-weight filter with a window-size of 0.95 d, which was found to be the optimal value during the SHERLOCK runs, and masked the transits corresponding to the candidate TOI-2257 b. We considered a synthetic planet to be recovered when its epoch was detected with 1 h accuracy and the recovered period was within 5% of the injected period. It is worth noting that since we injected the synthetic planets in the PDC-SAP light curve, the signals were not affected by the PDC-SAP systematic corrections; therefore, the detection limits should be considered as the most optimistic scenario (see, e.g., Pozuelos et al. 2020; Eisner et al. 2020).

In particular, we explored the $R_{\mathrm{planet}}-P_{\mathrm{planet}}$ parameter space in the ranges of $0.5–3.5\,R_\oplus$ with steps of $0.2\,R_\oplus$, and 1.0–30.0 d with steps of 1.0 d. For each pair $R_{\mathrm{planet}}-P_{\mathrm{planet}}$ we used four different phases. Hence, we analyzed a total of 1920 scenarios. The results, shown in Fig. 7, allowed us to rule out planets with sizes

---

[4] The SHERLOCK (Searching for Hints of Exoplanets from Lightcurves of space-based seekers) code is fully available on GitHub: https://github.com/franpoz/SHERLOCK

[5] The MATRIX ToolKit (Multi-phase Transits Recovery from Injected exoplanets Toolkit) code is available on GitHub: https://github.com/martindevora/tkmatrix
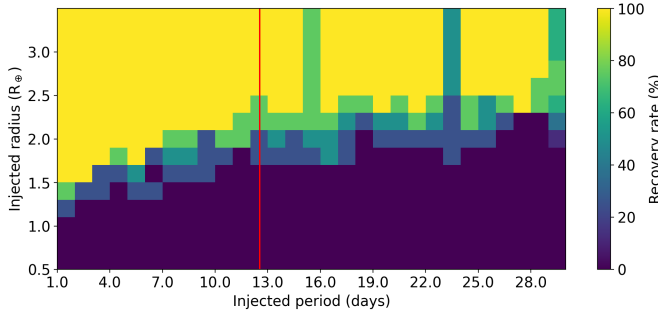
Fig. 7. Injection-and-recovery tests performed on TESS data to check the detectability of extra planets in the system. We explored a total of 1920 different scenarios. Each pixel evaluated four scenarios, that is, four light curves with injected planets having different P_{planet}, R_{planet} and T_0. Larger recovery rates are presented in yellow and green, while lower recovery rates are shown in blue and darker hues. We can rule out the presence of planets with sizes $>2.5\,R_\oplus$. Planets with sizes $<1.5\,R_\oplus$ would remain undetected. Planets with sizes between 1.5 and 2.5 $R_\oplus$ have recovery rates ranging from 30 to 70%. The red vertical line marks the maximum orbital period (12.54 d) allowed for the hypothetical inner planet to avoid crossing orbits between the planets. See the text for more details.

$>2.5\,R_\oplus$, with recovery rates larger than 80% for almost the full range of periods explored. On the other hand, planets with sizes $<1.5\,R_\oplus$ would remain undetected. In addition, we found that planet sizes $1.5 < R_\oplus < 2.5$ might be challenging to detect, with recovery rates ranging from 30 to 70 %.

It is important to notice that with the current data set, our models for TOI-2257 b presented in Sect. 4 favored an eccentric orbit. As such, there are forbidden periods for the hypothetical inner planet to avoid crossing orbits between the planets. In particular, safe orbits have a semimajor axis lower than the periastron distance for TOI-2257 b ($q = 0.073$ au). That is, the allowed orbital periods would be $\lesssim 12.54$ d. This limit in the orbital period for the hypothetical inner planet is displayed in Fig. 7 with a vertical red line.

6.2. SAINT-EX + Artemis photometry

As shown previously using TESS photometry, it would be challenging to find small planets with sizes $\leq 1.5\,R_\oplus$. Accordingly, we monitored TOI-2257 using the SPECULOOS network located in the Northern Hemisphere. This high-precision photometry allows us to detect single transits of Earth-size planets orbiting M dwarfs (Delrez et al. 2018; Murray et al. 2020; Demory et al. 2020; Niraula et al. 2020). Outwith the two transits shown in Sect. 2.2.3 we followed up the star for 93.5 h. These time-series observations were analyzed by our automatic pipelines as described in Murray et al. (2020) and Demory et al. (2020) in the search for transit events. We did not find any hint of transit-like features during this time. Hence, this negative result allowed us to rule out the presence of Earth-size planets for a range of orbital periods by computing the phase coverage; that is, we computed the percentage of phase covered for each orbital period from 0.1 to 15 d, in intervals of 0.01 d, for a total of 1500 periods. We found that because of day-night cycles only very short periods are fully covered in phase by our observations, as shown in Fig. 8. Indeed, only for orbital periods of ≤ 3.78 d was more than 80% of the orbit explored, meaning that periods equal to or shorter than this would most likely be detected if the planet existed and transited. For larger orbital periods, the phase
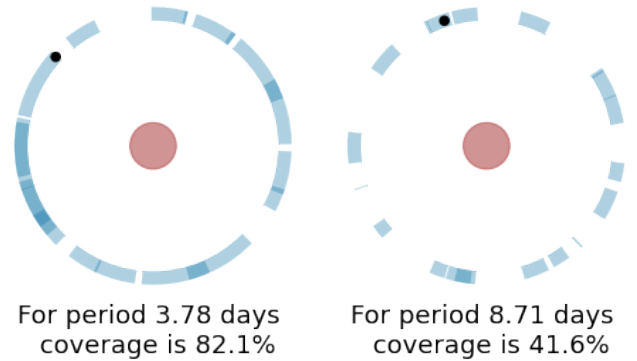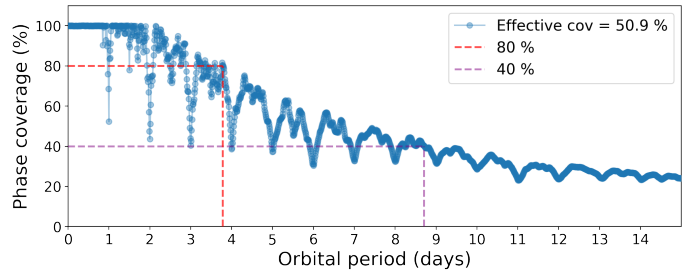
Fig. 8. Phase coverage for SAINT-EX and Artemis data. *Top*: evolution of the phase coverage of a hypothetical planet orbiting TOI-2257 as a function of the period, derived from SAINT-EX and Artemis observations (blue dots). The effective phase coverage is the integral of the phase coverage over the 0.1–15 day period range and is equal to 59%. The dotted red (purple) line indicates the period above which the phase coverage is always inferior to 80% (40%), which corresponds to the period of 3.78 days (8.71 days). We note that periods equal to an integer number of days are significantly less covered due to day-night cycles in ground-based observations. *Bottom*: graphical visualization of the coverage of TOI-2257 with SNO and SAINT-EX for a hypothetical planet with orbital periods of 3.78 and 8.71 days, respectively. Each blue circular arc represents one night of observation; its size is proportional to the number of hours observed each night, and a full circle depicts a duration of 3.78 (8.71) days.

coverage decreases rapidly to a minimum of 20% for the highest orbital period explored, 15 d.

7. Discussion

7.1. Composition

The radius of TOI-2257 b is $2.194^{+0.113}_{-0.111}\,R_\oplus$. Not having RV measurements, we used the relation of Chen & Kipping (2017) to estimate the likely mass, providing a wide range of predicted values centered around $5.7\,M_\oplus$. Using mass-radius curves from Zeng et al. (2016), it is expected that the planet's density is consistent with a composition of an ice or gas giant rather than a denser rocky body.

7.2. Eccentricity

Not having RV measurements, the eccentricity reported here is derived from the transit itself. In particular, it is driven by the transit duration, which can be degenerate with the impact parameter. Nevertheless, as the eccentric case is statistically favored over the circular case, we explore the system using the resulting eccentricity of $e = 0.496^{+0.216}_{-0.133}$. The high eccentricity of this object, shown in context in Fig. 9, provides a clue to the dynamic history of the system. Single-planet systems tend to
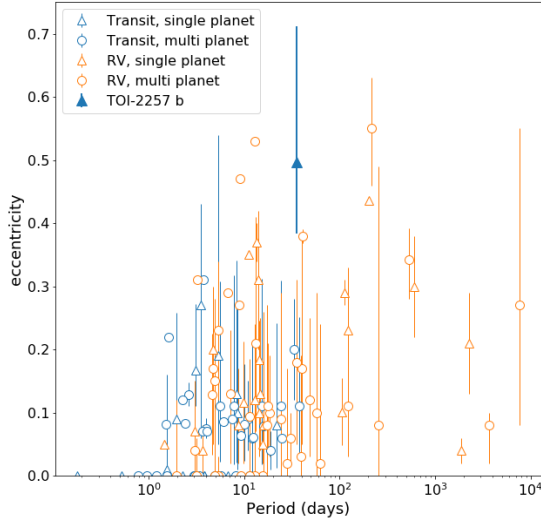
Fig. 9. Period and eccentricities for known planets orbiting M-dwarf stars ($T_{eff} < 3700$). TOI-2257 b, shown with a dark marker and thick error bar for emphasis, is the most eccentric transiting planet with only one known planet in the system. Data were retrieved from the Exoplanet Archive (https://exoplanetarchive.ipac.caltech.edu/); we note that systems without reported eccentricity errors are shown without error bars.

have dynamically hotter orbits with larger eccentricities than those in multi-planet systems (Xie et al. 2016; Van Eylen et al. 2019; Masuda et al. 2020). The high eccentricity of nearly 0.5 seen in TOI-2257 b is suggestive of the possible influence of a long-period giant planet rather than self-excitation, the latter of which Van Eylen et al. (2019) found to only explain eccentricities of up to around 0.3. An example of this mechanism was found for GJ 1148 b, a Saturn-mass planet orbiting an M dwarf in an eccentric orbit of ~0.38 (Haghighipour et al. 2010). Posterior observations found that an outer giant planet was responsible for exciting GJ 1148 b (Trifonov et al. 2018). TOI-2257 b's system parameters are consistent with the paradigm presented by Huang et al. (2017), in which systems that survive scattering by an outer giant planet show lower multiplicity and higher eccentricity. Future RV measurements would help to test this interpretation by searching for a massive planet in a more distant and likely non-transiting orbit.

7.3. Prospects for radial velocity observations

In order to constrain the mass of TOI-2257b, high-resolution spectroscopy with a precision of ~$1 \, \mathrm{m \, s^{-1}}$ or less is needed. Demangeon et al. (2021) showed in the case of the M3V-star L 98-59, the mass of a planet with a $2 \, \mathrm{m \, s^{-1}}$ semi-amplitude can be constrained with about 10% precision, taking the intrinsic stellar RV jitter into account. TOI-2257b is >3 mag fainter than L 98-59, and thus the RV precision is reduced to about $6{-}10 \, \mathrm{m \, s^{-1}}$ for a 900 s exposure with a state-of-the art instrument such as ESPRESSO at the VLT (Pepe et al. 2021). Current and upcoming infrared spectrographs such as CRIRES (Dorn et al. 2014), SPIROU (Donati et al. 2020), or NIRPS (Wildi et al. 2017), will be able to obtain a higher signal-to-noise, but the RV precision will still not allow direct measurement of the reflex motion of TOI-2257. However, the newly commissioned MAROON-X instrument (Seifahrt et al. 2020) at the Gemini-North telescope is expected to achieve a signal of $1 \, \mathrm{m \, s^{-1}}$ for TOI-2257. Combining the instrument noise with an estimated
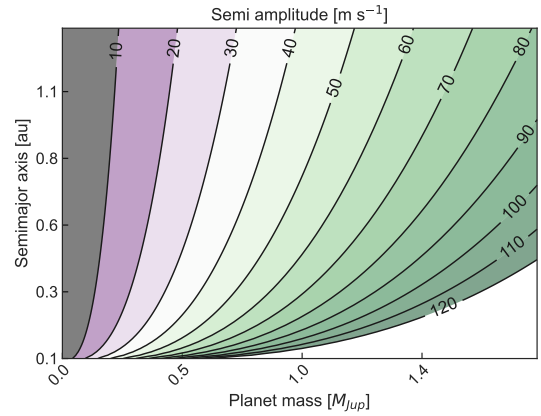
Fig. 10. Expected semi-amplitude of a possible giant planet orbiting TOI-2257 for different orbits and planetary masses.

stellar jitter of $1.5 \, \mathrm{m \, s^{-1}}$, it would be possible to constrain the mass to within 6σ after 26 measurements with the red arm and an exposure time of 20 min.

Even without high-precision instruments, lower-precision RV follow-up might result in the detection of a more massive planet that is not transiting or farther out and, thus, not visible in the current photometric data set. We explored this possible case since the presence of such a planet might cause the eccentricity of TOI-2257 b. As shown in Fig. 10, a giant planet with $1 \, M_{Jup}$ and orbiting in 1 au would result in an RV signal of about $50 \, \mathrm{m \, s^{-1}}$ with an orbital period of 640 days. The magenta and green areas in Fig. 10 show that the detection of an outer massive planet will be challenging but possible for current high-resolution instruments. The expected long periods of such planets would require continuous monitoring over the course of months to several years with high-precision spectrographs.

7.4. Prospects for atmospheric characterization

The long orbit of Planet b (35.9 days) makes it a rare object among currently known sub-Neptunes and, thus, a compelling target to study for its atmospheric composition and to gain clues about its formation and evolution. The planet's low time-averaged equilibrium temperature (Méndez & Rivera-Valentín 2017) of $T_{eq} = 256^{+61}_{-17} \, \mathrm{K}$ (assuming zero albedo and full day-night heat redistribution) along with the star's relative proximity to Earth (57.79 pc) and optical and NIR brightness (K-mag 10.67) strongly favors transmission spectroscopy. For example, JWST's transmission spectroscopy metric (TSM) is 32.71, following Kempton et al. (2018).

Thus, TOI-2257 b could be an interesting target to study ocean loss on this class of temperate sub-Neptunes. Probing O_3 abundances with red-sensitive JWST observations as well as O_2 abundances with ground-based optical observations from the Extremely Large Telescopes (ELT; Luger & Barnes 2015; Serindag & Snellen 2019), or probing CO and O_4 features (Schwieterman et al. 2016), could give clues in this regard.

Finally, TOI-2257 b is one of only ~20 currently known, characterizable sub-Neptunes whose equilibrium temperatures fall into a liquid-water-is-possible zone (Fig. 11). Of course, such exoplanets do not allow surface habitability, given their immense atmospheric pressure and heated surface. However, life in the clouds could be a possibility – as first proposed by Morowitz & Sagan (1967); Sagan & Salpeter (1976) and recently discussed for sub-Neptune-sized exoplanets by Seager et al. (2021) (see
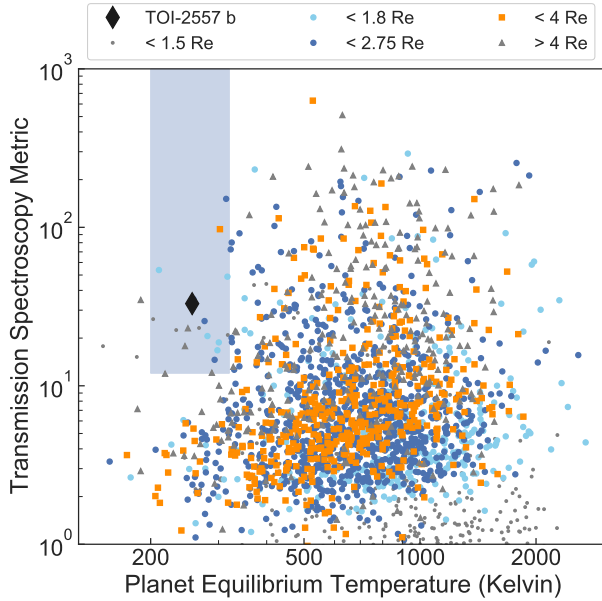
Fig. 11. TOI-2257 b and known exoplanets in the context of their equilibrium temperature (x axis) and TSM (y axis). Different symbols and colors designate different planet size categories. TOI-2257 b lies in the middle of the blue shaded area, which highlights sub-Neptunes (i) that are amenable for atmospheric characterization (TSM > 12) and (ii) for which life in the clouds is possible (T_{eq} between 200 and 320 K, following Seager et al. 2021). Equilibrium temperatures were estimated using an albedo of 0 and an emissivity of 1, following Kempton et al. (2018). Altering the assumptions for albedo and emissivity (e.g., assuming an albedo of 0.3, as for Earth and Neptune) adds lower error bars of ~10% and upper error bars of ~30% to the shown temperatures. Data were retrieved from the Exoplanet Archive (https://exoplanetarchive.ipac.caltech.edu/) on 2021 July 30. The figure has been adapted from Seager et al. (2021).

also Fig. 11). Additionally, this temperature regime could favor the surface habitability conditions of any potential exomoons, as discussed in the following section.

7.5. Prospects of exomoons orbiting TOI-2257 b

Moons in the Solar System are invaluable puzzle pieces for understanding our system formation history, evolution, and even habitability (see, e.g., Öpik 1960; Laskar et al. 1993; Rufu et al. 2017; Orgel et al. 2018). Equally valuable is studying moons hosted in other planetary systems, that is, exomoons. Indeed, due to the large number of moons orbiting Solar System planets, the possible existence of moons orbiting exoplanets is widely accepted. However, despite efforts to find them (see, e.g., Kipping et al. 2012, 2015; Hippke 2015; Teachey & Kipping 2018; Kreidberg et al. 2019), at the time of writing no detection has yet been confirmed.

One of the major interests of exomoons is their potential habitability. Indeed, massive rocky exomoons orbiting temperate giant planets have been suggested as places where life might arise and evolve over long timescales (see, e.g., Williams et al. 1997; Kaltenegger 2010; Heller & Barnes 2013, 2015; Heller et al. 2014). In particular, temperate moon–planet systems hosted by low-mass stars are widely discussed in the literature, providing arguments in favor and against the existence and habitability of exomoons. For example, it has been suggested that such moons will be likely tidally locked to the planet, a situation that would favor a uniform distribution of irradiation (Trifonov et al.
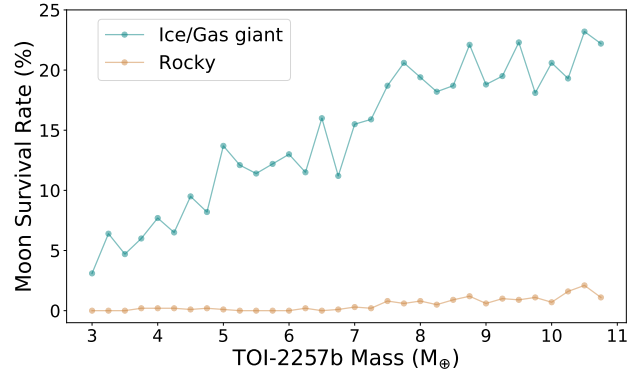
Fig. 12. MSR upper limit around TOI-2257 b as a function of the planetary mass. The blue line represents the solution when considering TOI-2257 b as a giant planet, while the yellow line is considering it as a rocky planet. Each data point is the MSR computed by simulating 1000 exomoons orbiting around TOI-2257 b, for a total of 64 000 scenarios tested.

2020). In addition, the magnetic field generated by the planet may protect the moon from the typical stellar flares produced by M dwarfs (Heller & Zuluaga 2013). These factors would mitigate some typical inconveniences when discussing the habitability of a planet orbiting in the habitable zone of an M dwarf (Khodachenko et al. 2007; Lammer et al. 2007). On the other hand, gravitational perturbations by the close star and extra planets in the system could induce eccentricities that would likely make any moon uninhabitable (Heller 2012). In any case, due to the number of currently unknown parameters, the field of habitable exomoons is still very speculative.

In this study we focus only on estimating the existence of rocky exomoons orbiting TOI-2257 b. To this end, we used dynamical considerations to compute the moon survival rate (MSR) following the formulation introduced by Sasaki et al. (2012) and the prescriptions given by Dobos et al. (2021). The simulation details are provided in Appendix B. The mathematical description takes into account tidal evolution in a star–planet–moon system. It is important to notice that this formulation assumes that the planet resides in a circular orbit around the host star; however, this is not the case for TOI-2257 b. Hence, the results yielded by our simulations should be considered as upper limits to the actual MSR as eccentric planetary orbits reduce the stability of the moon–planet systems.

The results of the simulations are displayed in Fig. 12. In summary, we found that the larger the mass of the planet, the larger the MSR, with a maximum MSR of about 20% for ice and gas giant planets. On the other hand, the MSR was almost null for the entire sample of possible planetary masses when considering a rocky planet. In reality, when increasing the planetary mass, the density also increases, passing from an ice and gas giant to a rocky planet. This change would happen between 5.5 and 6.5 $M_\oplus$, which, combined with the planetary radius of 2.194 $R_\oplus$, yields a planetary density of 2.9–3.5 g cm^{-3}. The MSR would follow the ice and gas giant solution until ~6 $M_\oplus$, dropping then to the estimated MSR for rocky planets. In such a case, the maximum MSR given for ~6 $M_\oplus$ is about 13%.

We conclude that TOI-2257 b is likely a single planet with a low probability of having any orbiting moons. This result is in line with those found by Sasaki et al. (2012) and Dobos et al. (2021), who established that it is very challenging for planets orbiting low-mass stars with a semimajor axis ≤0.2 au to harbor moons in stable orbits.

8. Conclusion

This work presents the discovery and characterization of TOI-2257 b, a sub-Neptune in a relatively long-period orbit around an M3V star. The preliminary characterization is based on photometry from TESS and several ground-based facilities, with spectral analysis and high-resolution imaging supporting the validation. TOI-2257 b occupies a sparsely populated region of parameter space. Currently, only two other transiting exoplanets around M dwarfs with periods greater than that of TOI-2257 b are known (Kepler-1652 b and TOI-700 d; Torres et al. 2017; Gilbert et al. 2020; Rodriguez et al. 2020). Furthermore, this single-planet system is the most eccentric planet transiting an M dwarf discovered to date, providing an opportunity to test possible formation scenarios.

While the expected driven reflex motion, on the order of a few m s^{-1}, makes current observations challenging, recent and upcoming instrumentation at observatories with larger collecting areas, such as MAROON-X at the Gemini Observatory and the HIRES spectrograph at the ELT (Marconi et al. 2021), will make it possible to obtain spectra for TOI-2257 with more than 20 times higher S/N than with ESPRESSO. Thus, these large telescopes will enable us to derive the mass of TOI-2257 b to within 10% and even allow us to search for possible other planets within the system. Regardless, this planet is one of only a small number of sub-Neptunes for which liquid water is a possibility. The expected TSM of the object makes it amenable to more detailed atmospheric characterization from JWST.

References

Agol, E., Luger, R., & Foreman-Mackey, D. 2020, AJ, 159, 123
Aller, A., Lillo-Box, J., Jones, D., Miranda, L. F., & Barceló Forteza, S. 2020, A&A, 635, A128
Alonso-Floriano, F. J., Morales, J. C., Caballero, J. A., et al. 2015, A&A, 577, A128
Astropy Collaboration (Robitaille, T. P., et al.) 2013, A&A, 558, A33
Astropy Collaboration (Price-Whelan, A. M., et al.) 2018, AJ, 156, 123
Badenas-Agusti, M., Günther, M. N., Daylan, T., et al. 2020, AJ, 160, 113
Bailer-Jones, C. A. L., Rybizki, J., Fouesneau, M., Mantelet, G., & Andrae, R. 2018, AJ, 156, 58
Baraffe, I., Homeier, D., Allard, F., & Chabrier, G. 2015, A&A, 577, A42
Barkaoui, K., Burdanov, A., Hellier, C., et al. 2019, AJ, 157, 43
Bonfils, X., Delfosse, X., Udry, S., et al. 2013, A&A, 549, A109
Borucki, W. J., Koch, D., Basri, G., et al. 2010, Science, 327, 977
Boss, A. P. 2001, ApJ, 551, L167
Brown, T. M., Baliber, N., Bianco, F. B., et al. 2013, PASP, 125, 1031
Buchner, J., Georgakakis, A., Nandra, K., et al. 2014, A&A, 564, A125
Casagrande, L., Flynn, C., & Bessell, M. 2008, MNRAS, 389, 585
Chen, J., & Kipping, D. 2017, ApJ, 834, 17
Choi, J., Dotter, A., Conroy, C., et al. 2016, ApJ, 823, 102
Cloutier, R., Rodriguez, J. E., Irwin, J., et al. 2020, AJ, 160, 22
Collins, K. A., Kielkopf, J. F., Stassun, K. G., & Hessman, F. V. 2017, AJ, 153, 77
Covey, K. R., Ivezić, Ž., Schlegel, D., et al. 2007, AJ, 134, 2398
Cutri, R. M., Skrutskie, M. F., van Dyk, S., et al. 2003, 2MASS All Sky Catalog of point sources
Cutri, R. M., Wright, E. L., Conrow, T., et al. 2021, VizieR Online Data Catalog: II/328
Daylan, T., Pinglé, K., Wright, J., et al. 2021, AJ, 161, 85
Delrez, L., Gillon, M., Queloz, D., et al. 2018, SPIE, 10700, 446
Demangeon, O. D. S., Zapatero Osorio, M. R., Alibert, Y., et al. 2021, A&A, 653, A41
Demory, B. O., Pozuelos, F. J., Gómez Maqueo Chew, Y., et al. 2020, A&A, 642, A49
Dobos, V., Charnoz, S., Pál, A., Roque-Bernard, A., & Szabó, G. M. 2021, PASP, 133, 094401
Donati, J. F., Kouach, D., Moutou, C., et al. 2020, MNRAS, 498, 5684
Dorn, R. J., Anglada-Escude, G., Baade, D., et al. 2014, The Messenger, 156, 7
Dotter, A. 2016, ApJS, 222, 8
Eisner, N. L., Barragán, O., Aigrain, S., et al. 2020, MNRAS, 494, 750
Espinoza, N., Kossakowski, D., & Brahm, R. 2019, MNRAS, 490, 2262

Feroz, F., Hobson, M. P., & Bridges, M. 2009, MNRAS, 398, 1601
Foreman-Mackey, D., Hogg, D. W., Lang, D., & Goodman, J. 2013, PASP, 125, 306
Foreman-Mackey, D., Luger, R., Agol, E., et al. 2021a, J. Open Source Softw., 6, 3285
Foreman-Mackey, D., Savel, A., Luger, R., et al. 2021b, exoplanet-dev/exoplanet v0.5.1
Gaia Collaboration (Prusti, T., et al.) 2016, A&A, 595, A1
Gaia Collaboration (Brown, A. G. A., et al.) 2018, A&A, 616, A1
Gaia Collaboration (Brown, A. G. A., et al.) 2021, A&A, 649, A1
Garcia, L. J., Timmermans, M., Pozuelos, F. J., et al. 2021, MNRAS, 509, 4817
Giacalone, S., Dressing, C. D., Jensen, E. L. N., et al. 2021, AJ, 161, 24
Gilbert, E. A., Barclay, T., Schlieder, J. E., et al. 2020, AJ, 160, 116
Gillon, M., Jehin, E., Magain, P., et al. 2011, EPJ Web Conf., 11, 06002
Goodman, J., & Weare, J. 2010, Commun. Appl. Math. Comput. Sci., 5, 65
Guerrero, N. M., Seager, S., Huang, C. X., et al. 2021, ApJS, 254, 39
Haghighipour, N., Vogt, S. S., Butler, R. P., et al. 2010, ApJ, 715, 271
Hauschildt, P. H., Allard, F., & Baron, E. 1999, ApJ, 512, 377
Hedges, C., Hughes, A., Zhou, G., et al. 2021, AJ, 162, 54
Heller, R. 2012, A&A, 545, L8
Heller, R., & Barnes, R. 2013, Astrobiology, 13, 18
Heller, R., & Barnes, R. 2015, Int. J. Astrobiol., 14, 335
Heller, R., & Zuluaga, J. I. 2013, ApJ, 776, L33
Heller, R., Williams, D., Kipping, D., et al. 2014, Astrobiology, 14, 798
Henden, A. A., Levine, S., Terrell, D., & Welch, D. L. 2015, AAS Meeting Abs., 225, 336.16
Hippke, M. 2015, ApJ, 806, 51
Hippke, M., & Heller, R. 2019, A&A, 623, A39
Hippke, M., David, T. J., Mulders, G. D., & Heller, R. 2019, AJ, 158, 143
Howell, S. B., Everett, M. E., Sherry, W., Horch, E., & Ciardi, D. R. 2011, AJ, 142, 19
Howell, S. B., Sobeck, C., Haas, M., et al. 2014, PASP, 126, 398
Howell, S. B., Everett, M. E., Horch, E. P., et al. 2016, ApJ, 829, L2
Huang, C. X., Petrovich, C., & Deibert, E. 2017, AJ, 153, 210
Jehin, E., Gillon, M., Queloz, D., et al. 2011, The Messenger, 145, 2
Jenkins, J. M. 2002, ApJ, 575, 493
Jenkins, J. M., Chandrasekaran, H., McCauliff, S. D., et al. 2010, SPIE Conf. Ser., 7740, 77400D
Jenkins, J. M., Twicken, J. D., McCauliff, S., et al. 2016, Proc. SPIE, 9913, 99133E
Jenkins, J. M., Tenenbaum, P., Seader, S., et al. 2020, Kepler Data Processing Handbook: Transiting Planet Search (USA: Kepler Science Document)
Jensen, E. 2013, Astrophysics Source Code Library [record ascl:1306.007]
Kaltenegger, L. 2010, ApJ, 712, L125
Kass, R. E., & Raftery, A. E. 1995, J. Am. Stat. Assoc., 90, 773
Kempton, E. M. R., Bean, J. L., Louie, D. R., et al. 2018, PASP, 130, 114401
Kesseli, A. Y., West, A. A., Veyette, M., et al. 2017, ApJS, 230, 16
Khodachenko, M. L., Ribas, I., Lammer, H., et al. 2007, Astrobiology, 7, 167
Kipping, D. M. 2013, MNRAS, 435, 2152
Kipping, D. M., Bakos, G. Á., Buchhave, L., Nesvorný, D., & Schmitt, A. 2012, ApJ, 750, 115
Kipping, D. M., Schmitt, A. R., Huang, X., et al. 2015, ApJ, 813, 14
Kreidberg, L. 2015, PASP, 127, 1161
Kreidberg, L., Luger, R., & Bedell, M. 2019, ApJ, 877, L15
Kumar, R., Carroll, C., Hartikainen, A., & Martin, O. A. 2019, J. Open Source Softw.
Lammer, H., Lichtenegger, H. I. M., Kulikov, Y. N., et al. 2007, Astrobiology, 7, 185
Laskar, J., Joutel, F., & Robutel, P. 1993, Nature, 361, 615
Lépine, S., Rich, R. M., & Shara, M. M. 2007, ApJ, 669, 1235
Li, J., Tenenbaum, P., Twicken, J. D., et al. 2019, PASP, 131, 024506
Luger, R., & Barnes, R. 2015, Astrobiology, 15, 119
Luger, R., Agol, E., Foreman-Mackey, D., et al. 2019, AJ, 157, 64
Mandel, K., & Agol, E. 2002, ApJ, 580, L171
Mann, A. W., Brewer, J. M., Gaidos, E., Lépine, S., & Hilton, E. J. 2013, AJ, 145, 52
Mann, A. W., Dupuy, T., Kraus, A. L., et al. 2019, ApJ, 871, 63
Masuda, K., Winn, J. N., & Kawahara, H. 2020, AJ, 159, 38
Massey, P., & Gronwall, C. 1990, ApJ, 358, 344
McCully, C., Volgenau, N. H., Harbeck, D.-R., et al. 2018, Proc. SPIE Conf. Ser., 10707, 107070K
Méndez, A., & Rivera-Valentín, E. G. 2017, ApJ, 837, L1
Morowitz, H., & Sagan, C. 1967, Nature, 215, 1259
Morton, T. D. 2015, Astrophysics Source Code Library [record ascl:1503.010]
Muirhead, P. S., Dressing, C. D., Mann, A. W., et al. 2018, VizieR Online Data Catalog: J/AJ/155/180
Murray, C. A., Delrez, L., Pedersen, P. P., et al. 2020, MNRAS, 495, 2446
Niraula, P., Wit, J. d., Rackham, B. V., et al. 2020, AJ, 160, 172
Nutzman, P., & Charbonneau, D. 2008, PASP, 120, 317
Öpik, E. J. 1960, MNRAS, 120, 404
Orgel, C., Michael, G., Fassett, C. I., et al. 2018, J. Geophys. Res. Planets, 123, 748
Parviainen, H. 2015, MNRAS, 450, 3233
Pepe, F., Cristiani, S., Rebolo, R., et al. 2021, A&A, 645, A96
Pozuelos, F. J., Suárez, J. C., de Elía, G. C., et al. 2020, A&A, 641, A23
Quinn, S. N., Becker, J. C., Rodriguez, J. E., et al. 2019, AJ, 158, 177
Rains, A. D., Žerjal, M., Ireland, M. J., et al. 2021, MNRAS, 504, 5788
Reiners, A., Zechmeister, M., Caballero, J. A., et al. 2018, A&A, 612, A49
Richer, H. B., Anderson, J., Brewer, J., et al. 2006, Science, 313, 936
Ricker, G. R., Winn, J. N., Vanderspek, R., et al. 2015, J. Astron. Teles. Instrum. Syst., 1, 014003
Rodriguez, J. E., Vanderburg, A., Zieba, S., et al. 2020, AJ, 160, 117
Rufu, R., Aharonson, O., & Perets, H. B. 2017, Nat. Geosci., 10, 89
Safonov, B. S., Lysenko, P. A., & Dodin, A. V. 2017, Astron. Lett., 43, 344
Sagan, C., & Salpeter, E. E. 1976, ApJS, 32, 737
Salvatier, J., Wiecki, T. V., & Fonnesbeck, C. 2016, PeerJ Comput. Sci., 2, e55
Sasaki, T., Barnes, J. W., & O'Brien, D. P. 2012, ApJ, 754, 51
Schlaufman, K. C., & Laughlin, G. 2010, A&A, 519, A105
Schwieterman, E. W., Meadows, V. S., Domagal-Goldman, S. D., et al. 2016, ApJ, 819, L13
Scott, N. J., Howell, S. B., Gnilka, C. L., et al. 2021, Front. Astron. Space Sci., 8, 138
Seager, S., Petkowski, J. J., Günther, M. N., et al. 2021, Universe, 7, 172
Sebastian, D., Gillon, M., Ducrot, E., et al. 2021, A&A, 645, A100
Seifahrt, A., Bean, J. L., Stürmer, J., et al. 2020, SPIE, 11447, 305
Serindag, D. B., & Snellen, I. A. G. 2019, ApJ, 871, L7
Skrutskie, M. F., Cutri, R. M., Stiening, R., et al. 2006, AJ, 131, 1163
Slesnick, C. L., Carpenter, J. M., & Hillenbrand, L. A. 2006, AJ, 131, 3016
Smith, J. C., Stumpe, M. C., Van Cleve, J. E., et al. 2012, PASP, 124, 1000
Speagle, J. S. 2020, MNRAS, 493, 3132
Stassun, K. G., & Torres, G. 2016, AJ, 152, 180
Stassun, K. G., & Torres, G. 2021, ApJ, 907, L33
Stassun, K. G., Collins, K. A., & Gaudi, B. S. 2017, AJ, 153, 136
Stassun, K. G., Corsaro, E., Pepper, J. A., & Gaudi, B. S. 2018a, AJ, 155, 22
Stassun, K. G., Oelkers, R. J., Pepper, J., et al. 2018b, AJ, 156, 102
Stassun, K. G., Oelkers, R. J., Paegert, M., et al. 2019, AJ, 158, 138
Stumpe, M. C., Smith, J. C., Van Cleve, J. E., et al. 2012, PASP, 124, 985
Stumpe, M. C., Smith, J. C., Catanzarite, J. H., et al. 2014, PASP, 126, 100
Teachey, A., & Kipping, D. M. 2018, Sci. Adv., 4, eaav1784
Theano Development Team 2016, ArXiv e-prints [arXiv:1605.02688]
Torres, G., Kane, S. R., Rowe, J. F., et al. 2017, AJ, 154, 264
Trifonov, T., Kürster, M., Zechmeister, M., et al. 2018, A&A, 609, A117
Trifonov, T., Lee, M. H., Kürster, M., et al. 2020, A&A, 638, A16
Twicken, J. D., Catanzarite, J. H., Clarke, B. D., et al. 2018, PASP, 130, 064502
Van Eylen, V., Albrecht, S., Huang, X., et al. 2019, AJ, 157, 61
Wells, R. D., Rackham, B. V., Schanche, N., et al. 2021, A&A, 653, A97
Wildi, F., Blind, N., Reshetov, V., et al. 2017, SPIE Conf. Ser., 10400, 1040018
Williams, D. M., Kasting, J. F., & Wade, R. A. 1997, Nature, 385, 234
Woolf, V. M., & Wallerstein, G. 2006, PASP, 118, 218
Wright, E. L., Eisenhardt, P. R. M., Mainzer, A. K., et al. 2010, AJ, 140, 1868
Xie, J.-W., Dong, S., Zhu, Z., et al. 2016, Proc. Natl. Acad. Sci., 113, 11431
Zeng, L., Sasselov, D. D., & Jacobsen, S. B. 2016, ApJ, 819, 127

¹ Center for Space and Habitability, University of Bern, Gesellschaftsstrasse 6, 3012 Bern, Switzerland
  e-mail: nicole.schanche@unibe.ch
² Astrobiology Research Unit, Université de Liège, Allée du 6 Août 19C, 4000 Liège, Belgium
³ Space Sciences, Technologies and Astrophysics Research (STAR) Institute, Université de Liège, Allée du 6 Août 19C, 4000 Liège, Belgium
⁴ Department of Physics, and Kavli Institute for Astrophysics and Space Research, Massachusetts Institute of Technology (MIT), Cambridge, MA 02139, USA
⁵ European Space Agency (ESA), European Space Research and Technology Centre (ESTEC), Keplerlaan 1, 2201 AZ Noordwijk, The Netherlands
⁶ Center for Astrophysics and Space Science, University of California San Diego, La Jolla, CA 92093, USA

[7] Instituto de Astrofísica de Canarias (IAC), Calle Vía Láctea s/n, 38200 La Laguna, Tenerife, Spain

[8] Universidad Nacional Autónoma de México, Instituto de Astronomía, AP 70-264, CDMX 04510, Mexico

[9] Universidad Nacional de Córdoba - Observatorio Astronómico de Córdoba, Laprida 854, X5000BGR, Córdoba, Argentina

[10] Consejo Nacional de Investigaciones Científicas y Técnicas (CONICET), Argentina

[11] Department of Earth, Atmospheric and Planetary Science, Massachusetts Institute of Technology, 77 Massachusetts Avenue, Cambridge, MA 02139, USA

[12] School of Physics & Astronomy, University of Birmingham, Edgbaston, Birmimgham B15 2TT, UK

[13] Department of Physics & Astronomy, Vanderbilt University, 6301 Stevenson Center Ln., Nashville, TN 37235, USA

[14] Jet Propulsion Laboratory, California Institute of Technology, 4800 Oak Grove Drive, MS 169-224, Pasadena, CA 91109, USA

[15] Oukaimeden Observatory, High Energy Physics and Astrophysics Laboratory, Cadi Ayyad University, Marrakech, Morocco

[16] Sternberg Astronomical Institute, Moscow State University (SAI MSU), Universitetskii pr. 13, Moscow 119991, Russia

[17] Physikalisches Institut, University of Bern, Gesellsschaftstrasse 6, 3012 Bern, Switzerland

[18] Center for Astrophysics | Harvard & Smithsonian, 60 Garden Street, Cambridge, MA, 02138, USA

[19] Observatoire de l'Université de Genève, Chemin des Maillettes 51, 1290 Versoix, Switzerland

[20] Caltech/IPAC, 1200 E. California Boulevard, Pasadena, CA 91125, USA

[21] Dpto. Física Teórica y del Cosmos, Universidad de Granada, 18071 Granada, Spain

[22] Department of Physics and Astronomy, University of New Mexico, 1919 Lomas Blvd NE, Albuquerque, NM 87131, USA

[23] NASA Exoplanet Science Institute, Caltech/IPAC, Mail Code 100-22, 1200 E. California Blvd., Pasadena, CA 91125, USA

[24] NASA Ames Research Center, Moffett Field, CA 94035, USA

[25] Universidad Nacional Autónoma de México, Instituto de Astronomía, AP 106, Ensenada 22800, BC, Mexico

[26] Department of Astronomy, University of Florida, Gainesville, FL, 32611, USA

[27] Department of Physics, University of Warwick, Gibbet Hill Road, Coventry CV4 7AL, UK

[28] Dept. of Physics & Astronomy, Swarthmore College, Swarthmore PA 19081, USA

[29] Department of Astronomy, Wellesley College, Wellesley, MA 02481, USA

[30] Cavendish Laboratory, JJ Thomson Avenue, Cambridge, CB3 0HE, UK

[31] NASA Goddard Space Flight Center, 8800 Greenbelt Road, Greenbelt, MD 20771, USA

[32] Department of Aeronautics and Astronautics, MIT, 77 Massachusetts Avenue, Cambridge, MA 02139, USA

[33] Department of Astrophysical Sciences, Princeton University, 4 Ivy Lane, Princeton, NJ 08544, USA

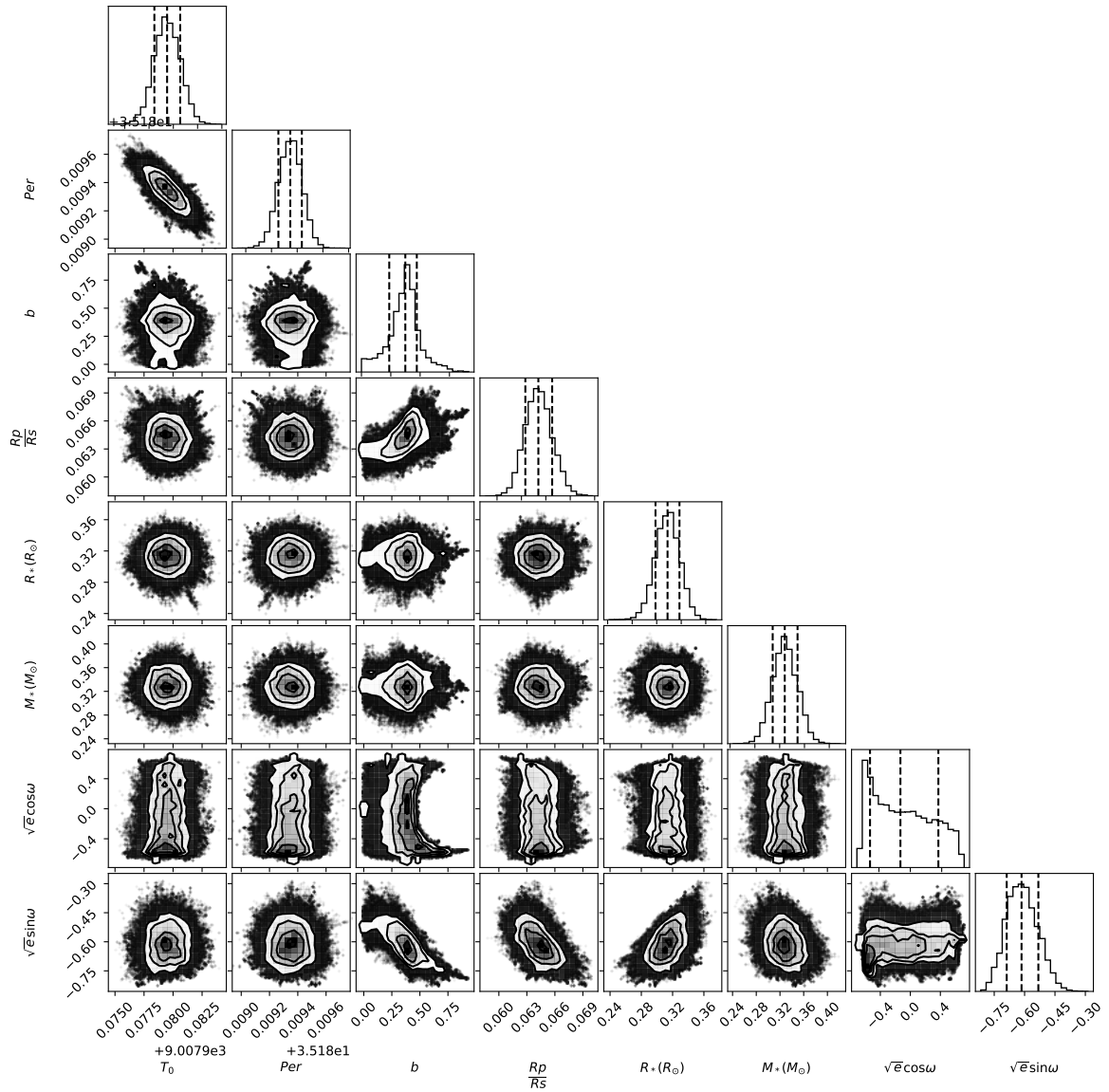## Appendix A: Posterior distribution of transit parameters

Fig. A.1. MCMC posterior distributions for the fit transit parameters. From left-to-right: Transit epoch (BJD−2,450,000), orbital period (d), impact parameter, planet-to-star radius ratio, stellar radius (R_*), stellar mass (M_*), $\sqrt{e}\cos\omega$, and $\sqrt{e}\sin\omega$.

Appendix B: Exomoon simulations

The main parameters that describe the stability of a moon are the planetary mass, radius, and semimajor axis, the quality factor that describes the dissipation energy Q_p, the rotational state, and the potential Love number k_{2p}.

In our case, only a few of these parameters are known: the planetary radius, R_p=2.194 $R_\oplus$, and semimajor axis, a_p=0.145 au. The other parameters are unknown. Hence, we explored them by taking into account the considerations described in detail by Dobos et al. (2021): (i) We explored the planetary mass, M_p, considering its uncertainty as given in Table 3, that is, ranging from 3 to 10.75 $M_\oplus$ in steps of 0.25 $M_\oplus$. (ii) The quality factor highly depends on the physical characteristics of the planet. It was established that for $R_p < 2.0$ $R_\oplus$ (rocky planets), $10<Q_p<500$, and for $R_p \geqslant 2.0$ $R_\oplus$ (ice and gas giant planets) with orbital periods larger than 10 d, $10^3<Q_p<10^6$, with the most probable value defined as $Q_p = 3 \times 10^4$. Our estimation of the planetary radius is R_p=2.194$^{+0.113}_{-0.111}$ $R_\oplus$, which is just within the limit between the given definition of rocky and ice and gas giant planets. To avoid as many biases as possible in our study, we ran two suites of simulations: one considering a rocky planet with $Q_p = 2.5 \times 10^2$ and the other considering an ice and gas giant with $Q_p = 3 \times 10^4$. (iii) The rotational spin of the planet was randomly explored between 10 h and 5 days. (iv) Finally, the potential Love number was assumed to be 0.299 for rocky planets and 0.5 for giant planets.

For each scenario, we generated a sample of 1000 moons whose stabilities were measured over a timescale of 1 Gyr. The parameters of moons we explored were: (i) the moon's mass, which was sampled randomly over the range (0.1–0.01)×M_p following a uniform distribution; (ii) the moon's density, which was explored following a Gaussian distribution with a mean value of ρ_m=3 g cm^{-3} and σ = 1/3 g cm^{-3}; and (iii) the moon's semimajor axis, a_m, which was chosen randomly from a uniform distribution between two times the Roche limit (R_{limit}) and the critical distance (C_d).

In each case, we monitored the dynamical evolution of the moon, prematurely finishing the integration if the moon collided with the planet or escaped from the system, that is, $a_m \leq R_{limit}$ or $a_m \geq C_d$, respectively. Then, the MSR was defined as the ratio of surviving moons (i.e., those that stayed in orbit around the planet until the end of the integration) and the number of tested configurations. In total, we explored 64,000 different scenarios. The results are explored further in the main text.